

AD-A273 020

2



246830-9-F

Final Report  
LONG-RANGE LASER IMAGING

J.C. Marron  
R.G. Paxman

September 1993

Prepared for:  
Phillips Laboratory/LIMI  
3550 Aberdeen Avenue, S.E.  
Kirtland AFB, NM 87117-5776

DTIC  
SELECTE  
NOV 22 1993  
S E D

Attn: Capt. G.L. Tarr

Contract Number : DLA900-88-D-0392 DO #35

93-28477



300

Approved for public release  
Distribution: FROTH



P.O. Box 134001  
Ann Arbor, MI 48113-4001

NOV 22 1993

REPORT DOCUMENTATION PAGE

Form Approved  
OMB No. 0704-0188

1a REPORT SECURITY CLASSIFICATION Unclassified		1b RESTRICTIVE MARKINGS	
2a SECURITY CLASSIFICATION AUTHORITY N/A		3 DISTRIBUTION/AVAILABILITY OF REPORT Approved for public release; distribution is unlimited.	
2b DECLASSIFICATION/DOWNGRADING SCHEDULE N/A			
4 PERFORMING ORGANIZATION REPORT NUMBER(S) 246830-9-F		5 MONITORING ORGANIZATION REPORT NUMBER(S)	
6a NAME OF PERFORMING ORGANIZATION ERIM	6b OFFICE SYMBOL (if applicable)	7a NAME OF MONITORING ORGANIZATION Phillips Laboratory	
6c ADDRESS (City, State, and ZIP Code) P.O. Box 134001 Ann Arbor, MI 48113-4001		7b ADDRESS (City, State, and ZIP Code) Kirtland AFB, NM 87117-5776	
8a NAME OF FUNDING /SPONSORING ORGANIZATION Phillips Laboratory	8b OFFICE SYMBOL (if applicable)	9. PROCUREMENT INSTRUMENT IDENTIFICATION NUMBER	
8c ADDRESS (City, State, and ZIP Code) Kirtland AFB, NM 87117-5776		10. SOURCE OF FUNDING NUMBERS	
		PROGRAM ELEMENT NO.	PROJECT NO.
		TASK NO.	WORK UNIT ACCESSION NO.
11 TITLE (Include Security Classification) Long Range Laser Imaging			
12. PERSONAL AUTHOR(S) Joseph C. Marron and Richard G. Paxman			
13a TYPE OF REPORT Final	13b. TIME COVERED FROM 1/93 TO 7/93	14. DATE OF REPORT (Year, Month, Day) 93/9/30	15. PAGE COUNT 66
16. SUPPLEMENTARY NOTATION			
17 COSATI CODES		18. SUBJECT TERMS (Continue on reverse if necessary and identify by block number) Active Imaging, Atmosphere, Absorption, Turbulence	
FIELD	GROUP		
19 ABSTRACT (Continue on reverse if necessary and identify by block number) This report summarizes a research program in which we evaluated the use of a Long-Range Laser Imaging (LRLI) system to perform the imaging tasks associated with laser target designation. The motivation for LRLI is to improve crew and aircraft survivability by increasing the standoff range, and reducing the required time interval, for air-based laser target designation. In this program we analyzed the capabilities of LRLI systems. We considered the signal level and its impact on sensor field-of-view. This analysis includes laser selection, atmospheric transmission, target reflectivity and optical system characteristics. It is shown that the laser signal level ultimately limits the number of target pixels. It is also shown that a pulsed system is required for background rejection. The impact of optical turbulence on system performance is also discussed. We evaluated the achievable resolution and considered the use of adaptive optics. It is shown, however, that severe anisoplanatism limits the utility of adaptive optics. We conclude that the most promising sensor design is based on conventional imaging and recommendations for proof-of-concept experiments are given.			
20 DISTRIBUTION/AVAILABILITY OF ABSTRACT <input checked="" type="checkbox"/> UNCLASSIFIED/UNLIMITED <input type="checkbox"/> SAME AS RPT <input type="checkbox"/> DTIC USERS		21. ABSTRACT SECURITY CLASSIFICATION Unclassified	
22a NAME OF RESPONSIBLE INDIVIDUAL ERIM		22b TELEPHONE (Include Area Code) (313) 994-1200	22c OFFICE SYMBOL

## CONTENTS

FIGURES .....	v
TABLES .....	vi
1.0 LONG-RANGE LASER IMAGING .....	1
1.1 INTRODUCTION .....	1
1.2 OVERVIEW .....	2
2.0 CONCEPT OF OPERATION .....	3
2.1 INTRODUCTION .....	3
2.2 LRLI APPLICATIONS .....	3
2.3 LRLI MISSIONS .....	5
3.0 SIGNAL LEVEL .....	9
3.1 INTRODUCTION .....	9
3.2 SIGNAL LEVEL .....	9
3.2.1 Laser Selection .....	9
3.2.2 Atmospheric Transmittance .....	11
3.2.3 Target Reflectivity .....	15
3.2.3 Optics .....	18
3.2.4 Received Photons .....	18
3.2.5 Background Level .....	19
3.3 REFERENCE .....	20
4.0 TURBULENCE PHENOMENOLOGY .....	21
4.1 INTRODUCTION .....	21
4.2 TURBULENCE THEORY .....	21
4.3 MODELS FOR INDEX STRUCTURE PARAMETER PROFILES ..	22
4.4 INDUCED PHASE ERRORS .....	23
4.5 ADAPTIVE CORRECTION OF PHASE ERRORS .....	31
4.6 INDUCED AMPLITUDE ERRORS .....	38
4.7 AERO-OPTICAL EFFECTS .....	39
4.8 CONCLUSIONS .....	41
4.9 REFERENCES .....	42

CONTENTS (Continued)

5.0 IMAGING SYSTEM CONCEPTUAL DESIGN ..... 43

    5.1 INTRODUCTION ..... 43

    5.2 CONVENTIONAL IMAGING ..... 43

    5.3 COMPENSATED IMAGING ..... 44

    5.4 SCANNER ..... 45

    5.5 PUPIL-PLANE IMAGING ..... 46

    5.6 RECOMMENDATION ..... 51

    5.7 REFERENCES ..... 51

6.0 LONG-RANGE DESIGNATOR PERFORMANCE ..... 53

    6.1 INTRODUCTION ..... 53

    6.2 PERFORMANCE PREDICTION ..... 53

    6.3 REFERENCE ..... 55

7.0 RECOMMENDATION FOR EXPERIMENTS ..... 57

    7.1 INTRODUCTION ..... 57

    7.2 PROOF-OF-CONCEPT EXPERIMENT LOCATION ..... 58

    7.3 REFERENCE ..... 59

Accession For	
NTIS CRA&I	<input checked="" type="checkbox"/>
DTIC TAB	<input type="checkbox"/>
Unannounced	<input type="checkbox"/>
Justification .....	
By .....	
Distribution/	
Availability Codes	
Dist	Avail and/or Special
A-1	

DTIC QUALITY INSPECTED 5

## FIGURES

2-1.	Illustration of LRLI Sensor . . . . .	4
2-2.	Illustration of Surveillance Mission . . . . .	5
2-3.	CFLOS Data for Various Locations . . . . .	6
2-4.	Illustration of CMT Detection Mission . . . . .	7
2-5.	DARPA Assessment of Search Requirements for a Variety of Targets . . . . .	8
3-1.	Factors that Dictate LRLI Signal Level . . . . .	9
3-2.	LOWTRAN Calculation for a Variety of Atmospheric Conditions . . . . .	12
3-3.	FASCODE Results for Spectral Regions of Interest . . . . .	14
3-4.	Goniometer Facility Used to Collect BRDF Data . . . . .	16
3-5.	Examples of BRDF Curves . . . . .	16
3-6.	Multispectral Signatures of Olive Drab Paint and Vegetation . . . . .	17
3-7.	Background Irradiance Levels for a Variety of Conditions . . . . .	19
4-1.	Index Structure Parameter Profiles Using Extended Hufnagel Model . . . . .	24
4-2.	Index Structure Parameter Profiles Using Empirical Model . . . . .	25
4-3.	Resolving Power as a Function of Aperture Diameter . . . . .	29
4-4.	Anisoplanatic Imaging . . . . .	32
4-5.	RMS Phase Error as a Function of Field Position . . . . .	34
5-1.	Block Diagram of Conventional LRLI Sensor . . . . .	43
5-2.	Block Diagram of Compensated LRLI Sensor . . . . .	44

FIGURES (Continued)

5-3.	Block Diagram of LRLI Scanner . . . . .	45
5-4.	Sensor Geometry . . . . .	47
5-5.	Illumination Pulse Timing . . . . .	50
6-1.	Illustration of Scenario for Long-Range Imaging . . . . .	53
6-2.	SNR for Laser Designator Versus Range in km . . . . .	55
7-1.	Block Diagram for Proof-of-Concept Experiment . . . . .	57
7-2.	Illustration of Possible Imaging Location from Mt. Haleakala . . . . .	58
7-3.	Illustration of Hot-Air Balloon Approach for LRLI Sensor Development . .	59

TABLES

3-1.	Laser Selection Factors . . . . .	10
3-2.	Boundary Layer Models Used for LOWTRAN Calculations . . . . .	11
3-3.	Atmospheric Absorption Coefficients for Some Specific Laser Wavelengths . . . . .	13
4-1.	Computed Values of $r_o$ and OTF Modulation at $r = .2m$ . . . . .	30
4-2.	Computed Values of $r_o$ , $R\alpha_o$ , and Various OTF Modulation . . . . .	36
4-3.	Computed Values of $r_o$ and Greenwood Frequency, $f_g$ . . . . .	38

# 1.0 Long-Range Laser Imaging

## 1.1 Introduction

This report summarizes a research program in which we evaluated the use of a Long-Range Laser Imaging (LRLI) system to perform the imaging tasks associated with laser target designation. The motivation for LRLI is to improve crew and aircraft survivability by increasing the standoff range, and reducing the required time interval, for air-based laser target designation. Current designator systems, such as LANTIRN and Pave Tack, use a thermal imaging system (FLIR) to identify targets and to perform other functions such as Bomb Damage Assessment (BDA). These designator systems are limited to a maximum stand-off range of roughly 15 km due to atmospheric absorption of thermal light and the unsatisfactory image resolution obtained with long-range thermal imaging. To increase the standoff range, one must consider alternatives to thermal imaging for use with laser designation systems.

With the LRLI approach, imaging and target designation are performed from a high-altitude platform at a long-range from the target. Imaging is performed by using active laser illumination instead of passive thermal imaging. We considered a platform altitude of roughly 13 km with the range to the target being roughly 100 km. Along with imaging, the LRLI platform would also aim a laser designator at the target. A close-range fighter aircraft then prosecutes the target without having to select an aim-point or perform Bomb-Damage Assessment (BDA). Therefore the time interval for which the fighter aircraft is at risk is significantly reduced.

Our program concerned analysis of how various phenomenologies affect the performance of an LRLI sensor. One conclusion of this study is that the sensor's Field-Of-View (FOV) is limited by the available laser power. For example, for an aircraft range of 100 km, a 20 J laser would allow an FOV that is roughly the size of a football field. The sensor would thus operate in a "soda-straw" imaging mode with sub-meter resolution over an FOV that encompasses a football field. While this FOV is sufficient for many tasks, it may be necessary to use multiple laser pulses to construct a mosaic image of a larger target area.

A second important conclusion of this study is that resolutions sufficient for LRLI missions can be achieved without adaptive optics. Our analysis shows that turbulence-induced aberrations for the particular path considered are not severe. The sensor can thus operate with a conventional imaging telescope.

The results of this study indicate that the LRLI sensor concept is feasible and that proof-of-concept experiments are warranted. The recommended experiment plan is to conduct mountain-top experiments with a pulsed IR laser and a range-gated focal-plane array.

## **1.2 Overview**

This report is divided into sections that describe various aspects of the LRLI system concept, relevant phenomenology and recommendations for proof-of-concept experiments. The first technical section, Section 2, describes the concept of operations for the LRLI sensor. Operational features of the sensor, and some specific missions are discussed.

Section 3 contains analysis of phenomenology that affects the signal strength and sensor FOV. Items considered include atmospheric transmittance and target reflectivity. Our analysis indicates that the laser transmittance in the Short-Wave IR (SWIR) band (1.0 - 2.5  $\mu\text{m}$ ) is best for the longer wavelengths in this band due to reduced aerosol scattering. We also found that the scattering loss occurs almost entirely within the boundary layer (lowest 2 km) of atmosphere.

In section 4 we discuss phenomenology associated with atmospheric turbulence. Specific aspects include induced phase error, anisoplanatism, scintillation, aero-optical phase error and the Greenwood frequency. The conclusion of our analysis is that adaptive optics (atmospheric correction) are not necessary because the induced phase errors are relatively mild. Furthermore, effects such as anisoplanatism and the high Greenwood frequency make adaptive optics impractical.

Section 5 contains analysis of four conceptual designs for LRLI imaging sensors. These include conventional imaging, compensated imaging, a scanner and pupil plane imaging. Based on the atmospheric turbulence phenomenology, it follows that the conventional imaging approach is the leading candidate for implementation.

The performance of long-range laser designator systems is considered in Section 6. We consider the energy received by a close-range laser weapon from long-range designation.

Finally, in Section 7, we give recommendations for proof-of-concept experiments for the LRLI sensor. We consider experiments conducted from a mountain top, hot-air balloon and aircraft. At this point it is evident that mountain-top experiments entail the lowest risk and expense and are the recommended approach.

## 2.0 Concept of Operation

### 2.1 Introduction

In this section of the report we discuss the concept of operations for the LRLI sensor. This discussion begins in Section 2.2 with an overview of the applications for the LRLI sensor. These applications include both surveillance and laser target designation. Some specific missions, which include threat identification and Critical Mobile Target (CMT) detection, are then discussed in Section 2.3.

### 2.2 LRLI Applications

The LRLI sensor can be viewed as an optical adjunct to the JSTARS platform. JSTARS, which is an acronym for Joint Surveillance and Target Attack Radar System, is a long-range radar surveillance platform. It has a synthetic aperture radar that can operate in wide area surveillance and Moving Target Indicator (MTI) modes. JSTARS was used very effectively in Operation Desert Storm. The LRLI sensor would augment the capabilities of JSTARS by providing high-resolution laser imagery from long ranges. In addition, the LRLI sensor would have the capability of laser target designation by illuminating a target point with a small diameter laser beam which is used as a beacon for a laser guided weapon.

The use of a long-range laser imager and target designator provides a potentially superior approach to current methods for targeting high-value objects. As illustrated in Fig. 2-1, the laser imager/designator would be located on a high-altitude (13 km) platform such as the JSTARS platform, or potentially the AirBorne Laser (ABL) platform. These platforms travel at roughly 450 knots. The target, which is at a range of between 50 - 100 km (or depression angles of  $4^{\circ}$  -  $15^{\circ}$ ), could be illuminated with two beams of laser light: a broad beam for active imaging and a narrow laser designator beam. The two beams are at different wavelengths. The designator beam provides a beacon for a laser guided weapon that is launched from another platform, or perhaps the ground. The key feature of this system is the increased survivability afforded by the long standoff-range. The key technical issues are (1) to produce a small designation spot in the presence of the turbulent atmosphere and (2) to achieve fine-resolution imaging at the long standoff.

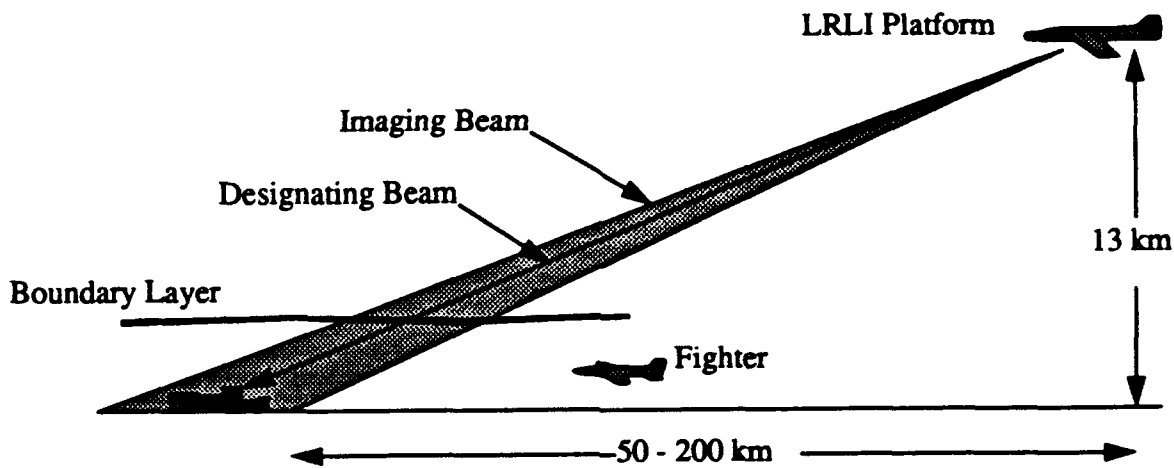


Figure 2-1. Illustration of LRLI Sensor.

Current methods for conducting high-value bombing missions include laser designators and smart autonomous missiles such as cruise missiles. Existing airborne laser designation systems include the Pave Tack and LANTIRN (Low Altitude Navigation and Targeting with Infrared at Night) systems. The LANTIRN system is the most modern and is currently flown on F-15E and F-16 aircraft. LANTIRN provides range information and stabilizes the laser beam on a target aim point for laser-guided weapons. The maximum range of this laser ranger/designator is roughly 15 km. Thus the LRLI concept would provide a significant increase in designation range.

During a typical bombing mission a crew using a LANTIRN pod must perform several tasks at close range to the target. First, they must recognize the cued target using a FLIR sensor. For some missions, particularly tactical scenarios, this recognition task must be accompanied by Identify Friend of Foe (IFF). The next task is aim-point selection. The laser designator is then locked onto the target and the laser-guided bomb is released. The designating laser beam must be maintained on the target during the entire timeline from initial ranging through weapon release to weapon impact. During this time the designating airframe and its crew are exposed to enemy counterfire. Once weapon impact occurs, the crew must continue to look at the target to perform BDA.

The most compelling reason to employ a long-range imager and designator as a follow-on for systems such as the LANTIRN pod is to enhance crew and aircraft survivability. In addition, the long-range platform can conduct IFF, aim-point selection, and BDA with improved efficiency.

The long-range designator approach also has advantages over the smart munition approach. The primary advantage is in the area of cost. So called smart and brilliant weapons are

being developed and deployed to find and destroy military targets. These weapons are complex machines which are expensive and currently have limited autonomous targeting capability. The LRLI approach places most of the processing power, machine as well as human, on a remote platform and allows the weapon to be relatively less smart and thus less expensive. In addition, many smart munitions are not reprogrammable whereas the long range designator can readily designate alternative targets.

### 2.3 LRLI Missions

In this section we discuss two example missions for the LRLI sensor. The first mission is pre-hostility surveillance which is illustrated in Fig. 2-2. The sensor platform would periodically fly a path along the border and the intentions of opposing forces would be determined by detecting changes in selected targets. The distance between the flight path and border is shown as 6 km to avoid threats such as anti-aircraft artillery. Note that in some cases a larger distance may be required. With the sensors range capability of roughly 100 km, one could image 94 km beyond the

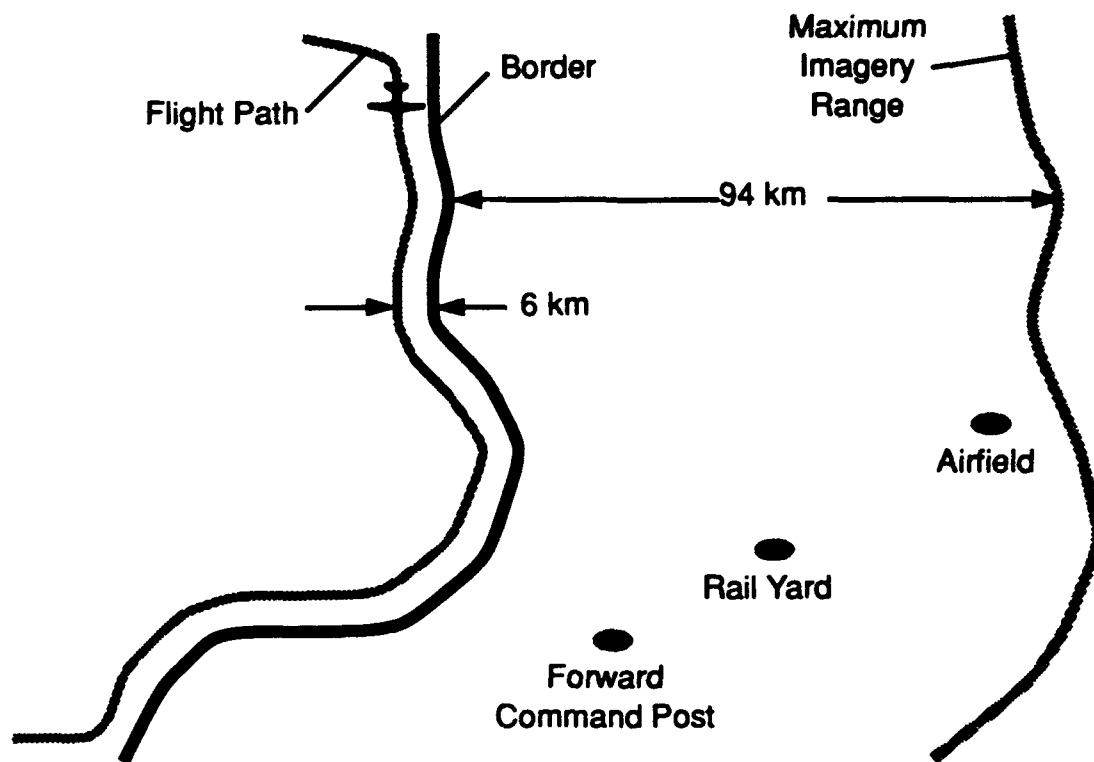


Figure 2-2. Illustration of Surveillance Mission.

border.

One feature of this mission is that aircraft navigation is challenging. The aircraft must remain clear of the border while maintaining sensor pointing accuracy. Pointing is compounded by the likely requirement for image mosaic capability. As discussed in Section 3, the LRLI sensor will have a limited FOV which is likely to be on the order of 100 m x 100 m. To image an airport which is typically 4 km x 4 km, a large number of images would have to be combined, or specific areas would have to be pre-selected.

While the LRLI sensor does have the capability for long-range, night-time imaging it also requires Cloud-Free-Line-Of-Sight (CFLOS) to the target. Figure 2-3 contains CFLOS data for 3 sites. These data were obtained from the Air Force Environmental Technical Applications Center at Scott AFB. Note that the probability of CFLOS is highly dependent on location and for some locations it is dependent on the season.

The second mission for which an LRLI sensor would be useful is Critical Mobile Target (CMT) detection. In this case the aircraft would be part of a precision strike package. The role of the LRLI platform would be to aid various fighter and bomber aircraft by finding and targeting CMTs. The LRLI aircraft would be assigned a specific area of responsibility and it would receive cues for threats in the area. The threat cue areas are in many cases several square kilometers and thus search or image mosaic capability would be required. Within the indicated area the LRLI sensor would be used to locate, identify and then designate the threat for a laser-guided weapon that would be delivered by a fighter aircraft that flies close to the target. As stated above, this

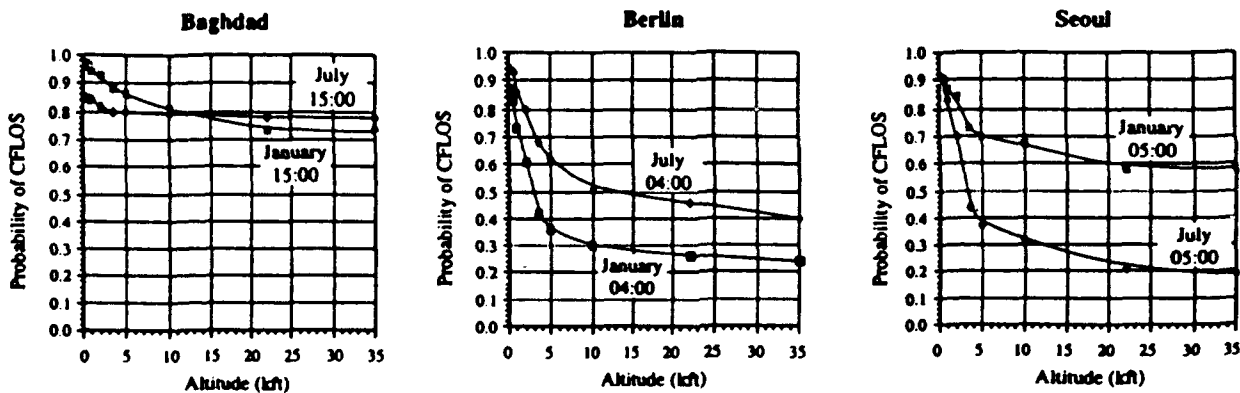


Figure 2-3. CFLOS Data for Various Locations.

reduces the responsibility of the fighter aircraft and increases crew and aircraft survivability. Survivability of the LRLI platform is ensured by having adequate stand-off range for the specific air-defense threat, and by having adequate escape time for the LRLI aircraft.

An example flight path for the CMT detection mission is shown in Fig. 2-4. It is envisioned that the aircraft would orbit at a safe distance from the border and periodically interrogate suspected SCUD, SRT and SAM sites. Fixed targets such as bridges could also be interrogated. Figure 2-5 contains a DARPA assessment of revisit rate and search requirements for a variety of mobile targets. The least demanding target is a ship in port which has a known location and must be interrogated only a few times a day. The most demanding type of target is a terrorist SCUD. These targets can be spread over a large area ( $10^5$  sq km) and they must be revisited at roughly 10 minute intervals. It is likely that in order to cover the large areas required for SCUD detection, other wide area search sensors would be required to aid the LRLI sensor by eliminating false alarms and further specifying areas for the LRLI sensor to interrogate. Once a target is found, the LRLI sensor would designate it and a laser guided weapon would be delivered by a fighter aircraft.

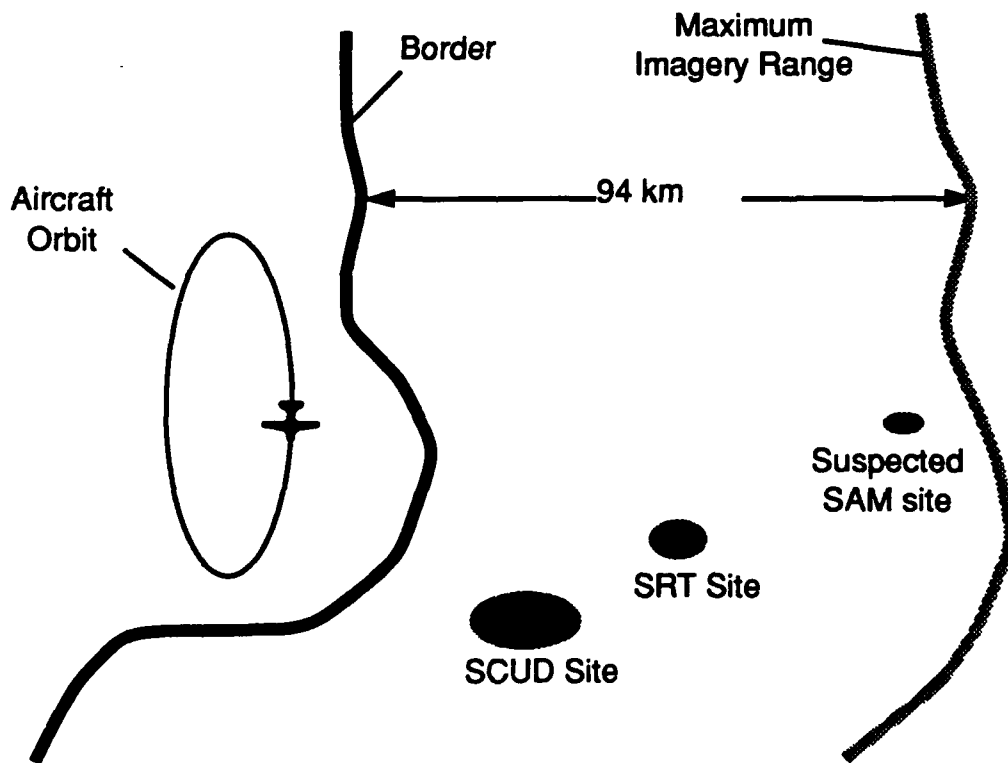


Figure 2-4. Illustration of CMT Detection Mission.

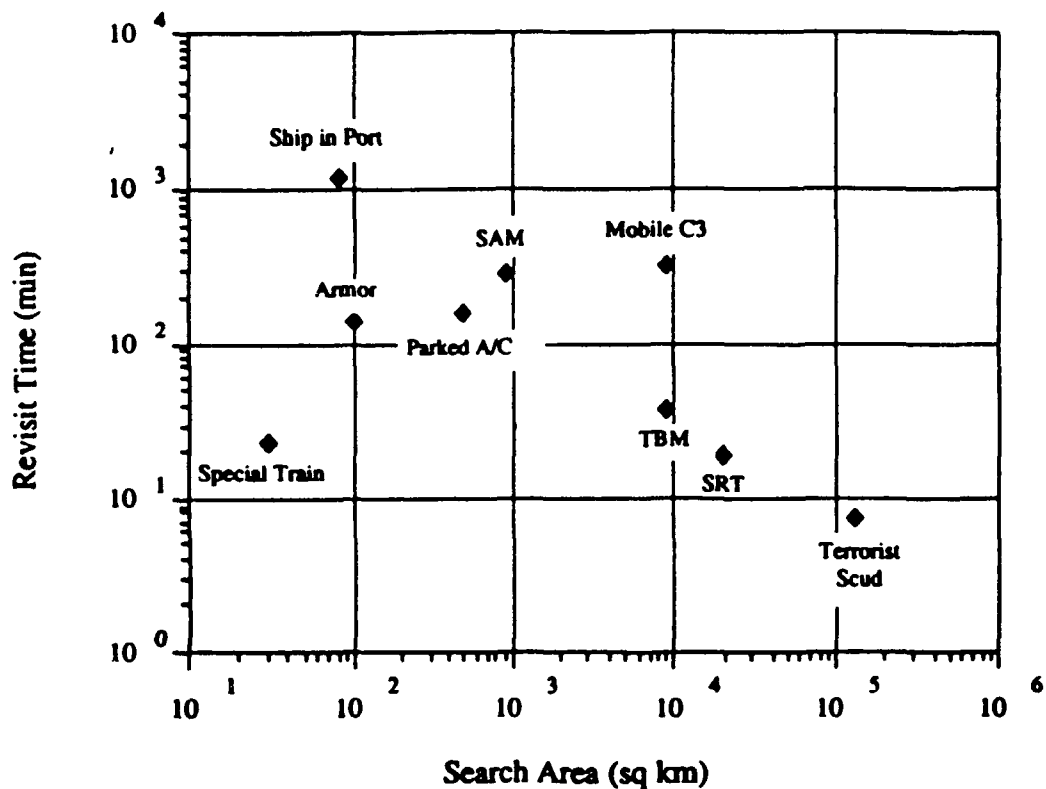


Figure 2-5. DARPA Assessment of Search Requirements for a Variety of Targets.

In summary the LRLI sensor has several useful capabilities which include; fine-resolution imaging, long-range surveillance, night-time operation and the ability determine the range to a target and designate it for delivery of a laser weapon. At the same time shortcomings of the LRLI sensor are the small FOV, precise pointing and navigation requirements and weather constraints. Despite these shortcomings, it is apparent that the LRLI sensor can play an important role in future military operations.

## 3.0 Signal Level

### 3.1 Introduction

In this Section of the report we discuss various aspects of the phenomenology that affect the signal level for an LRLI sensor. Also, based on the phenomenology, we make recommendations for certain components of the LRLI system. In Section 3.2 we discuss items that limit the signal level and sensor FOV. These include laser selection, atmospheric transmittance, target reflectivity, background irradiance and properties of the optical system. This discussion leads ultimately to a parameterized expression for the number of received photons per image pixel.

### 3.2 Signal Level

The ability to perform long-range laser imaging is limited primarily by the  $1/R^2$  dependence of the return signal level, where  $R$  is the aircraft to target range. In addition to this factor, other important factors are shown in Fig. 3-1. These factors are addressed in consecutive subsections below.

#### 3.2.1 Laser Selection

The selection of a laser for the LRLI sensor is based on a trade-off between a variety of properties that include laser power, wavelength, coherence length, beam quality, waveform (pulse

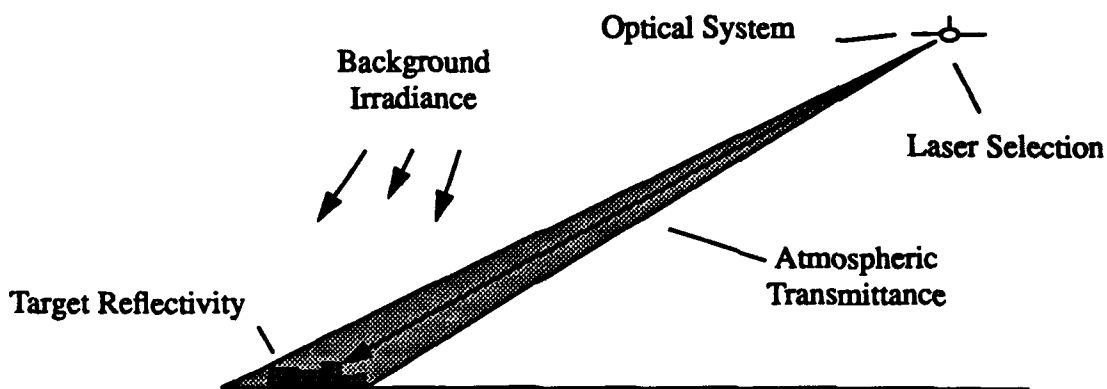


Figure 3-1. Factors that Dictate LRLI Signal Level.

repetition rate and pulse length) and cost. The laser must also be flyable. The purpose of this section is to describe laser selection factors and make a recommendation on laser selection.

The various laser selection factors are summarized in Table 3-1. The comments apply specifically to the LRLI program.

**Table 3-1: Laser Selection Factors**

Laser Property	Comment
Power	Power must be sufficient to give desired return per pixel, and desired FOV. Power of 20 - 100 J per pulse is initial estimate for imaging laser.
Wavelength	Wavelength is driven by phenomenology (atmospheric transmittance, etc.), resolution requirements and eye safety. Range of 1.5- 2.1 $\mu\text{m}$ is desirable.
Coherence Length	Requirement is dependent on imaging mode; conventional imaging requires little coherence, while non-conventional (pupil-plane) imaging requires long coherence. Laser design is simplified, and output power is increased, with reduced coherence.
Beam Quality	High beam quality (1 - 2 xDL) is required for designator beam, less beam quality for imaging beam.
Waveform	Laser must be pulsed to reduce background contribution. High repetition rate is desirable, but is limited by laser average power.
Cost	For demonstration experiments laser should be low cost, commercially available.
Flyability	Laser must fit within size, weight and power budget. Hazard to operator must be minimized.

Many lasers can be considered for this application. Candidates include solid-state lasers, ion lasers, dye lasers and more exotic lasers such as chemical oxygen iodine, deuterium fluoride, and free-electron. It is apparent, however, that solid-state lasers are the prime candidates. Examples include Nd: YAG (with Raman Shifting), Nd:YLF, Thulium:YAG, Ho:YAG and several others. These lasers offer a wide range of wavelengths and high-powered, diode-pumped versions are becoming available. For example, a 275 W diode pumped Nd:YAG laser is discussed in Ref. 3.1.

### 3.2.2 Atmospheric Transmittance

The performance of the LRLI sensor is influenced by atmospheric transmittance. Most importantly, the sensor requires cloud-free-line-of-sight (CFLOS). Even with CFLOS, the performance will vary greatly with changing atmospheric conditions. In this program we have evaluated two aspects of atmospheric transmittance; broadband transmittance (LOWTRAN) and narrow-band transmittance (FASCODE). With LOWTRAN one can determine general features of the atmospheric absorption and thus determine regions of the spectrum where long-range laser imaging is feasible. To evaluate specific laser lines, FASCODE is used to determine the transmittance.

For the atmospheric path considered here, atmospheric absorption and scattering takes place mainly in the boundary layer, which is the lowest 2 km portion of the atmosphere and furthermore, most of this light loss is attributable to scattering. Thus the amount of the path that exists below 2 km has great impact on the light loss. As a result, the LRLI optical path is considerably less lossy than a near-ground horizontal path of the same length. Also, because the loss is a function of altitude for the LRLI path, absorption calculations must be conducted for the entire path rather than using a single Beer's law coefficient, which is valid for a horizontal path.

For the LOWTRAN computations we used the LOWTRAN7 model. With this we evaluated the broadband atmospheric transmittance for a 100 km slant-range path that extends from an altitude of 13 km to the ground. This evaluation includes both absorption and scattering effects and it uses the 1976 US standard atmospheric model. We computed the transmittance for the boundary layer (0-2 km altitude) aerosol models listed in Table 3-2. In addition we used the default troposphere, stratosphere and upper-atmosphere models.

**Table 3-2: Boundary Layer Models Used for LOWTRAN Calculations.**

model type	visibility	wind/season
desert	75 km	wind = 0
rural 23	23 km	spring-summer
maritime	23 km	spring-summer
rural 5	5 km	spring-summer
urban	5 km	fall-winter

The results of LOWTRAN calculations are shown in Fig. 3-2. The plots serve as a guide for laser wavelength selection and the different curves correspond to various atmospheric condi-

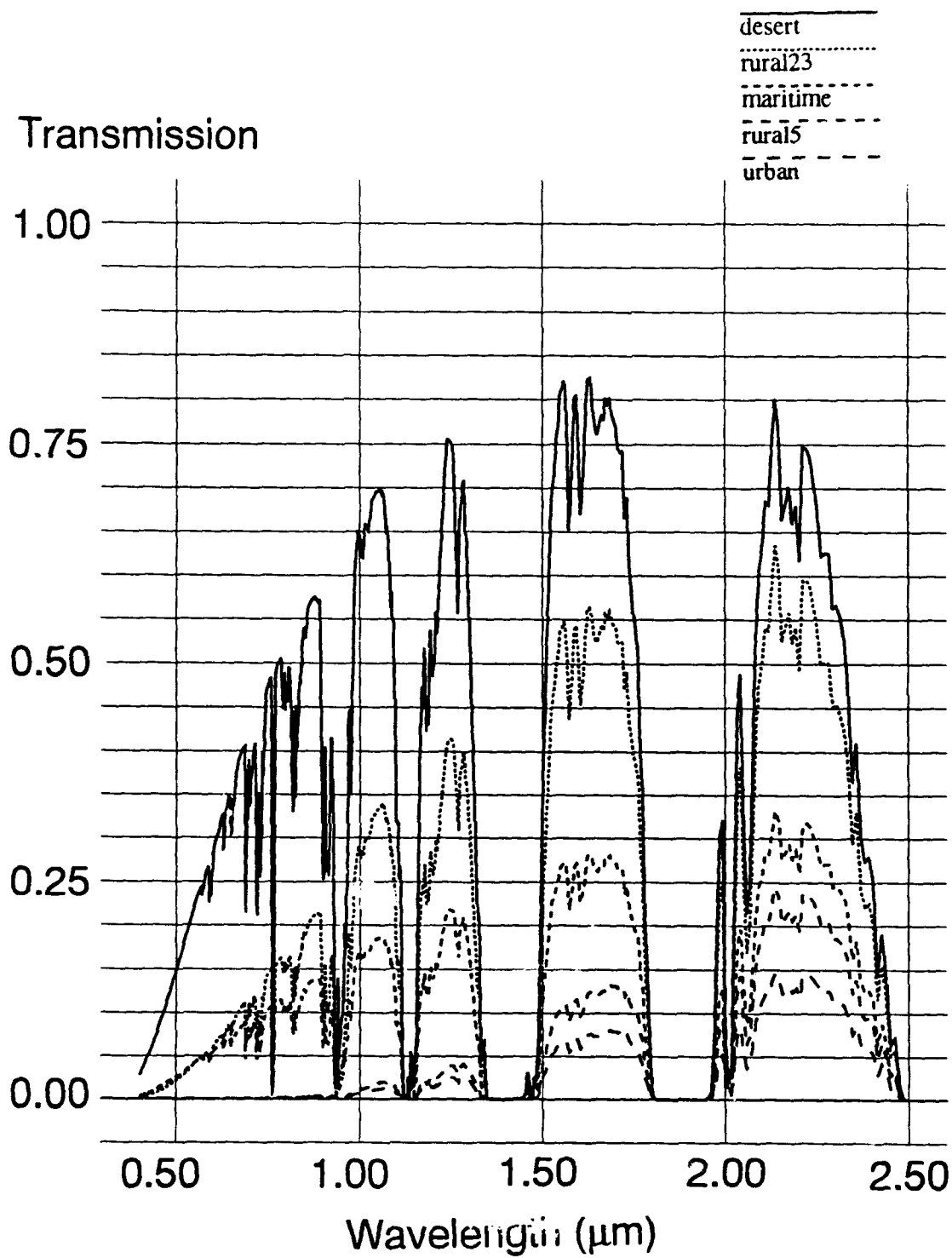


Figure 3-2. LOWTRAN Calculations for a Variety of Atmospheric Conditions.

tions. Notice that these curves have pronounced dips particularly at 1.4  $\mu\text{m}$  and 1.85  $\mu\text{m}$ ; these dips are water bands and are caused by light absorption of water vapor. These curves do indicate that there are several regions that are suitable for operation, however, notice that for the less transmissive atmospheres, the longer wavelengths are favored. This is because Mie scattering from large particles such as fog and pollutants has a tendency to be less severe at longer wavelengths. Under these conditions operation in the 2.1 region is favored. We also did FASCODE calculations for the same 100 km slant range path for some specific spectral regions. These results are given in Fig. 3-3. The computations were done in the vicinities of laser lines at 1.06  $\mu\text{m}$  (Nd:YAG), 1.54  $\mu\text{m}$  (Raman shifted Nd:YAG) and 2.10  $\mu\text{m}$  (Ho:YAG). These computations were done only for the "Rural 23 km Visibility" slant path atmosphere. The results for other atmospheres can be extrapolated from these. Notice that in all cases the transmission is very good. Also note that these results are in good agreement with the LOWTRAN results given above; FASCODE does reveal absorption detail, however the average absorption levels are captured by LOWTRAN. One can expect that similar agreement exists for the other boundary-layer atmospheres.

Fascode calculations were also done to determine the attenuation for a 1km horizontal path at zero altitude. These calculations allow us to determine the absorption constant per kilometer of boundary layer of atmosphere. These results can then be used to evaluate attenuation for longer paths within the boundary layer by using Beer's law. The absorption for a path of length  $L$  km is thus given by  $\alpha = \exp[-\kappa L]$ . Note that the pathlength must be within the boundary layer. The resulting coefficients are given in Table 4-3. Calculations based on these coefficients as compared to long path results indicate that the atmospheric absorption occurs almost entirely within the boundary layer of the atmosphere. To roughly compute atmospheric absorption for a long path, one can determine the length of the path that is within the boundary layer and use the Beer's law absorption for this path to approximate the absorption for the entire path.

**Table 3-3: Atmospheric Absorption Coefficients for Some Specific Laser Wavelengths.**

Wavelength	Absorption per km
1.06 $\mu\text{m}$ (Nd:YAG)	0.0670
1.54 $\mu\text{m}$ (Raman Shifted Nd:YAG)	0.0438
2.10 $\mu\text{m}$ (Ho:YAG)	0.0335

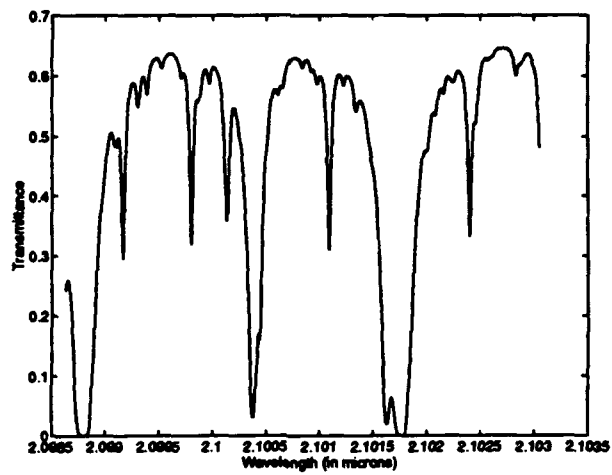
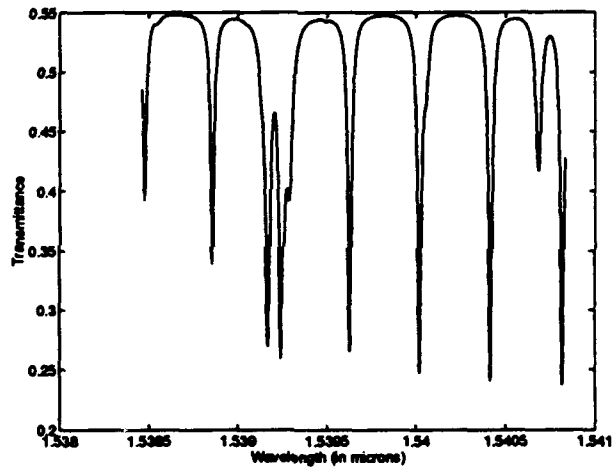
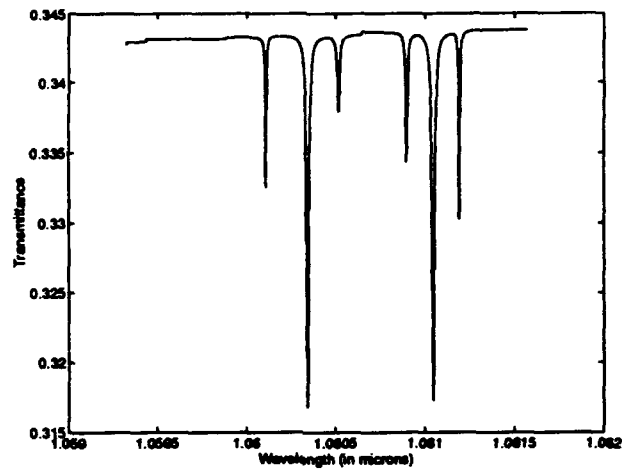


Figure 3-3. FASCODE Results for Spectral Regions of Interest.

### 3.2.3 Target Reflectivity

An important aspect of LRLI phenomenology is the characterization of target and background material properties. These properties include: reflectivity, multispectral properties and polarization properties. The Bidirectional Reflectance Distribution Function (BRDF) data is a key element for determination of these properties. For laser based sensors, with the source and receiver in proximity, it follows that standard monostatic BRDF data is required. This data is collected by placing a sample of a particular target or background material on a goniometer as illustrated in Fig. 3-4. A laser at the desired wavelength then illuminates the material and a detector with a small aperture in proximity to the laser measures the return level. The detector output is then recorded as the angle of the target is changed using the goniometer.

The mathematical definition of BRDF is

$$\rho = \frac{L_r}{E_i}$$

where  $L_r$  is the reflected radiance and  $E_i$  is the incident irradiance. The units of BRDF are inverse steradian. The value of the BRDF thus allows one to calculate the amount of light reflected by a surface, per steradian of receiver aperture, for a given incident power per unit area. Because the data is given as a function of sample tilt angle, one can compute signature levels for a variety of geometries. Some example BRDF curves are shown in Fig 3-5. These curves were taken using a Nd:YAG laser operating at  $1.06\mu\text{m}$ . The left curve is for a particular olive drab paint that is a specular reflecting material as indicated by the peaked BRDF curve. Note that not all olive drab paints are this specular. The center curve is for vegetation, which is relatively diffuse giving the flat curve. The curve on the right is for a net, which is also a diffuse reflector. An important aspect of target reflectivity is whether or not the scattered light is depolarized. BRDF data is typically collected using a polarized laser and measurements are made with co- and cross-polarizers in front of the detector. As shown in Fig. 3-5, the diffuse material depolarized the light while the specular material retains polarization which is evidenced by the disparity of the curves. These results do correspond to the trend that specular materials retain polarization. Furthermore, at longer wavelengths, materials tend to be specular.

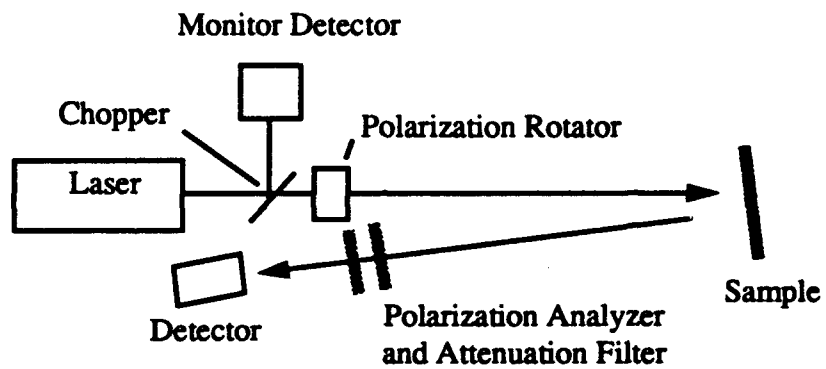


Figure. 3-4. Goniometer Facility Used to Collect BRDF Data.

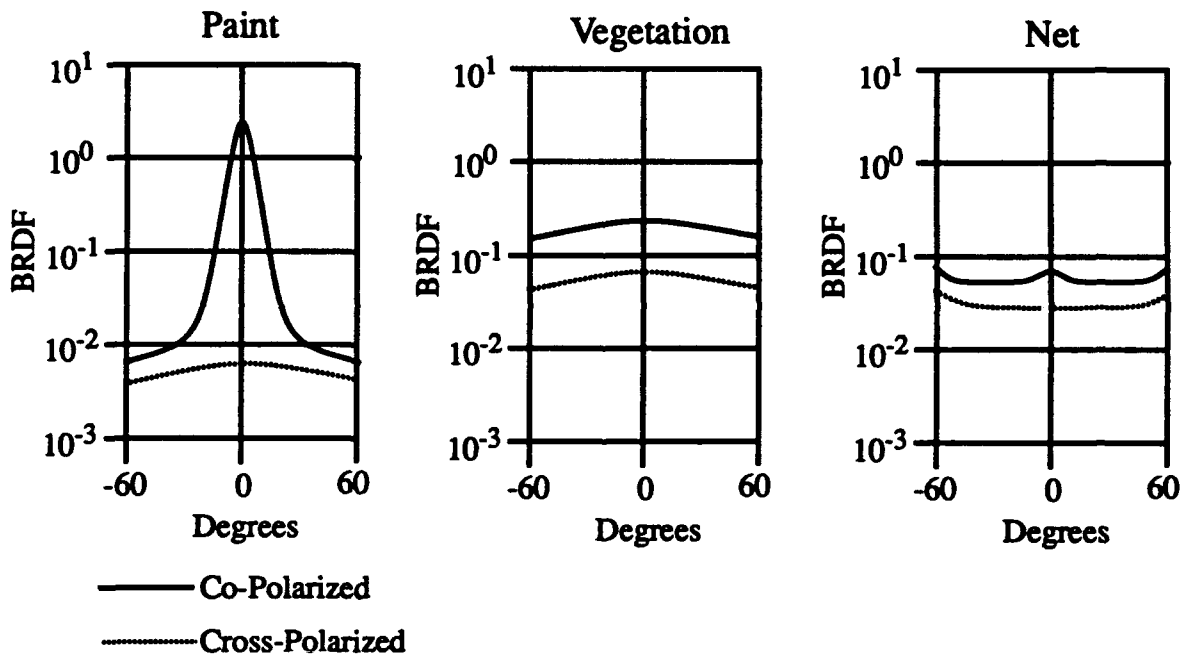


Figure. 3-5. Examples of BRDF Curves.

Targets also exhibit spectral variation in their reflectivity. The multispectral signatures of Olive Drab (OD) paint and vegetation are shown in Fig. 3-6. The different signatures were collected for a number of samples and the mean values plus and minus one standard deviation are shown. Note from these curves that the vegetation is expected to have a higher reflectivity value than OD paint at 1.06  $\mu\text{m}$ , while at 2.1  $\mu\text{m}$  the reflectivity is lower than that for the OD paint. This dip in the reflectivity of the vegetation is associated with its water absorption.

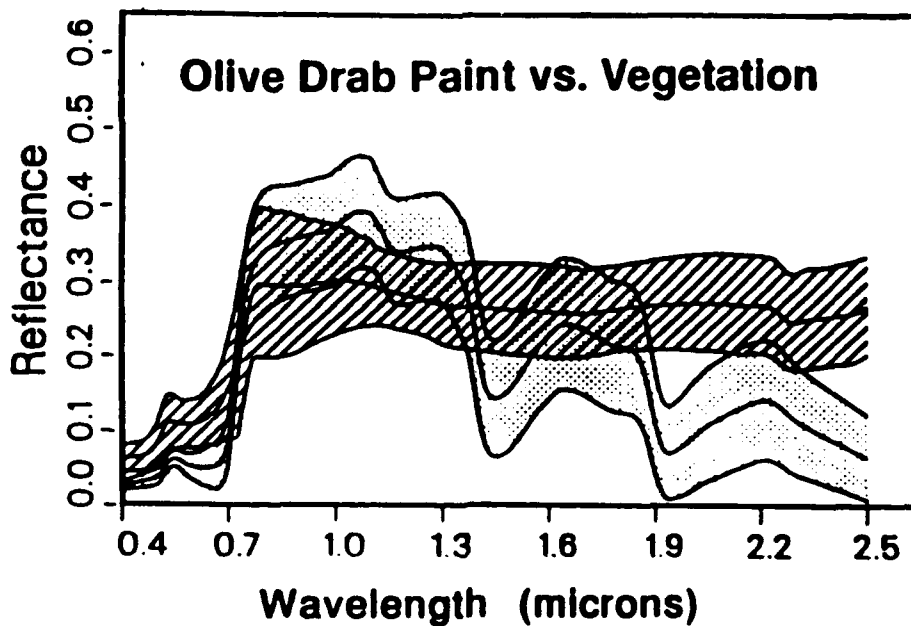


Figure 3-6. Multispectral Signatures of Olive Drab Paint and Vegetation. Olive drab paint is denoted by cross-hatched region.

### 3.2.3 Optics

The optical system has a large impact on the signal level that is delivered to the sensor focal plane. Perhaps the most important parameter is the aperture size, which should be maximized. Note, however, that having a large aperture on an air platform is not trivial. In addition the transmission of the optical system must also be considered. In general simpler optical systems, such as conventional imaging systems, will have significantly better transmission than more complicated systems such as compensated imaging systems.

### 3.2.4 Received Photons

The number of photons received by a pixel in a long range laser imaging system is given by

$$N = \frac{EA\lambda\rho\tau_o\tau_a^2}{R^2hc}$$

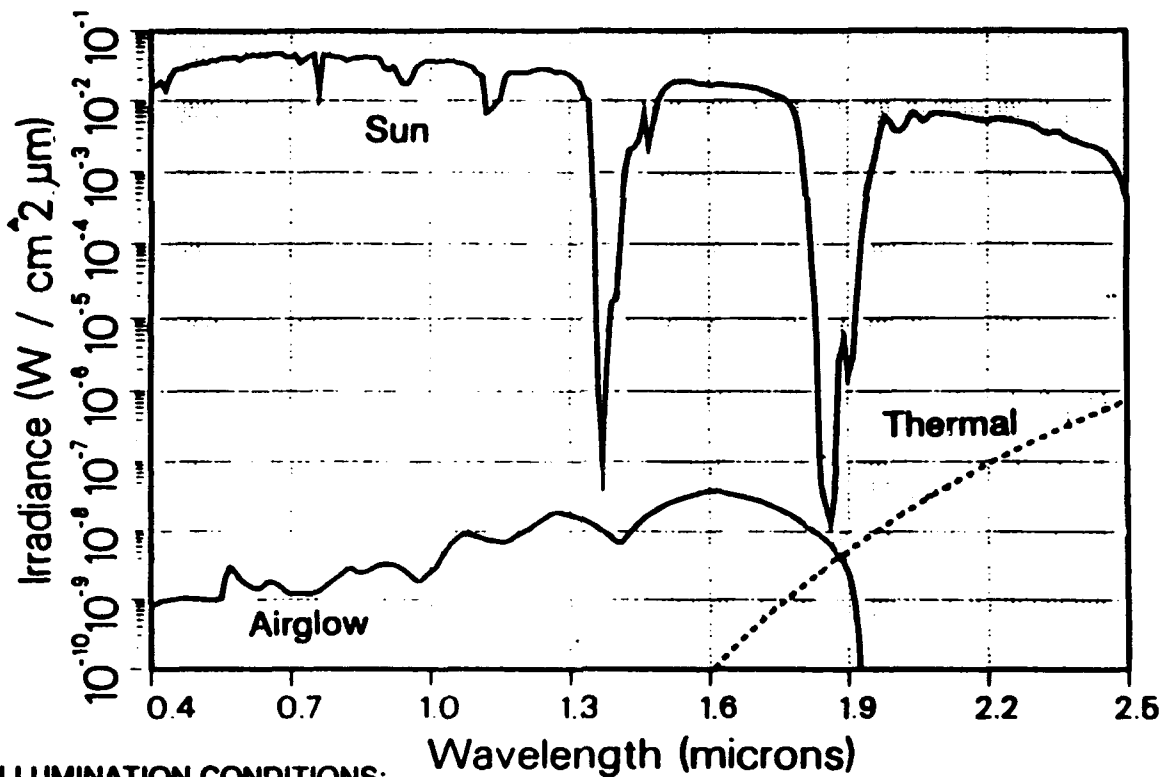
where parameters and their values are;

$E = 2 \times 10^{-3} \text{ J}$	laser energy per target pixel (20 J total / $10^4$ pixels)
$A = 0.5 \text{ m}^2$	aperture area
$\lambda = 1 \text{ } \mu\text{m}$	laser wavelength
$\rho = 0.1$	target BRDF
$\tau_o = 0.5$	optics transmission
$\tau_a = 0.1$	atmospheric transmission
$R = 100 \text{ km}$	range
$hc = 2 \times 10^{-25}$	

For these parameter values it follows that  $N = 250$  photons per pixel. It follows that the noise level is given roughly by  $(N)^{1/2}$ , which gives an SNR of roughly 16.

### 3.2.5 Background Level

For robust operation the LRLI signal level must be greater than the signal from the background irradiance of the ground. Figure 3-7 gives background irradiance levels for a variety of backgrounds. To compare these irradiance values to the laser irradiance levels let us assume that the received light is filtered through a standard 10 nm spectral filter and that the return is range gated with a 1  $\mu$ sec duration. For the full sun condition (evaluated at 1.3  $\mu$ m), the resulting 1 m<sup>2</sup> pixel with 1 msec integration time is  $E_B = 2 \times 10^{-6}$  J / (m<sup>2</sup>  $\mu$ sec 10 nm). This background irradiance level is three orders of magnitude lower than the laser irradiance level which is  $E_L = 2 \times 10^{-3}$  J. Note that this ratio is even more favorable for other illumination conditions. If, however a CW laser is used the situation is reversed and the background is significantly greater than the laser illumination. Thus it is essential that the LRLI sensor operate in a pulsed mode for background rejection.



ILLUMINATION CONDITIONS:

Sun: subarctic summer, 30° from zenith

Airglow: NVL Canada data (no clouds, no moon, time 20:00, 10/13/68)

Thermal: 287°K blackbody, emissivity=1

Figure 3-7. Background Irradiance Levels for a Variety of Conditions.

### 3.3 Reference

- [3.1] B. Comaskey, et al. "Diode pumped 275 Watt Average Power Nd:YAG Slab Laser," Proc. SPIE Vol. 1627, 122-126 (1992).

## 4.0 Turbulence Phenomenology

### 4.1 Introduction

The Long-Range Laser-Imaging (LRLI) concept involves imaging ground scenes at a range of about 100 *Km* from an airborne platform at an altitude of about 13 *Km*. The radiation used for imaging must pass through the turbulent atmosphere, a process that will induce aberrations in the imagery. Although the strength of the atmospheric turbulence may be mild near the sensor (because of the high altitude), the relatively long path that the radiation takes through the atmosphere suggests that these aberrations can be significant. Furthermore, radiation originating from different points in the scene can traverse significantly different atmospheric paths. Thus, anisoplanatic effects are expected to be significant as well. The purpose of this section is to investigate the effects of atmospheric turbulence in the LRLI scenario.

An excellent review article by Roddier [4.1] on astronomical imaging through atmospheric turbulence will provide the interested reader with a thorough tutorial on many of the concepts discussed here. Our objective is to provide a high-level review of concepts that are critical to analyzing the LRLI problem.

### 4.2 Turbulence Theory

Atmospheric air flow is nearly always turbulent. In fully-developed turbulence, the kinetic energy in large-scale motions is converted to smaller and smaller scale motions until the energy is dissipated into heat by viscous friction. Since atmospheric temperature is a function of altitude, turbulent mixing of the atmosphere creates inhomogeneities in the temperature. The index of refraction for a small atmospheric volume depends upon the temperature, pressure, humidity, and wavelength. We are particularly interested in fluctuations in the index of refraction, since these contribute to phase aberrations. Spatial variations in the index of refraction depend primarily on spatial variations in temperature. The spatial statistics of the temperature or the index of refraction are usually characterized by a structure function:

$$D_f(\boldsymbol{r}) = \langle |f(\boldsymbol{r}' + \boldsymbol{r}) - f(\boldsymbol{r}')|^2 \rangle, \quad (4-1)$$

where  $f(\mathbf{r})$  is a stochastic process defined on the vector  $\mathbf{r}$  and the angle brackets represent an ensemble average. In the Kolmogorov theory of turbulence, the temperature structure function is locally isotropic and has the form

$$D_t(r) = C_t^2 r^{2/3}, \quad (4-2)$$

where  $C_t^2$  is the temperature structure parameter,  $r \equiv |\mathbf{r}|$ , and  $r$  is restricted to lie in a range extending from a few millimeters to a few meters. Similarly, the index of refraction structure function is given by

$$D_n(r) = C_n^2 r^{2/3}, \quad (4-3)$$

where  $C_n^2$  is the index structure parameter. This parameter is a measure of the effect of the turbulence on optical propagation. In practice, temperature measurements are used to determine the temperature structure parameter which then yields the index structure parameter according to

$$C_n^2 = \left( \frac{\partial n}{\partial t} \right)^2 C_t^2. \quad (4-4)$$

### 4.3 Models for Index Structure Parameter Profiles

The index structure parameter is a function of altitude, meteorological conditions, and time of day. The effect of the turbulence upon an optical system will depend upon the specific realization of the index structure parameter altitude profile. A good deal of effort has been directed at modeling these profiles in order to predict imaging performance. A model that is frequently used and agrees reasonably well with experimental data is the Hufnagel model [4.2,4.3].

$$C_n^2(h) = 8.2 \times 10^{-56} v^2 h^{10} \exp\{-h/1000\} + 2.7 \times 10^{-16} \exp\{-h/1500\}, \quad (4-5)$$

where  $h$  is the altitude above sea level in meters and  $v$  is the root-mean square wind speed in the upper-atmosphere (between 5 and 20 Km) in meters/sec (typically  $27 \pm 9m/s$ ). In the lower atmosphere a much stronger variability occurs due to the diurnal cycle and meteorological conditions. Hufnagel's model can be extended at lower altitudes with an  $h^{-4/3}$ ,  $h^{-1}$ , and  $h^{-2/3}$  dependence to represent unstable, neutral, and unstable conditions, respectively. This

extended Hufnagel model is consistent with observations [4.1]. Extended Hufnagel model  $C_n^2$  profiles are presented in Figure 4-1.

Although the Hufnagel model is widely used, there is considerable variability between modeled and measured  $C_n^2$  profiles. A useful compilation of measured  $C_n^2$  profiles is available in reference [4.4]. These data, along with additional published data (such as from [4.2]), were used to derive minimum, average, and maximum values of  $C_n^2$  as a function of height. The resulting empirical  $C_n^2$  profiles are presented in Figure 4-2. These profiles illustrate the variability that can occur in  $C_n^2$  measurements. We believe that a performance estimate based solely on average behavior is insufficient since atmospheric turbulence is so variable. A performance estimate should at least include an estimate for poor conditions (maximum  $C_n^2$  profile). It should be remembered that the data used to create the empirical curves were all collected at astronomical sites at night, perhaps giving an optimistic bias to the curves. Therefore, it is likely that the turbulence will even be worse than predicted by the maximum curve on occasion.

#### 4.4 Induced Phase Errors

When a spherical wave propagates through a volume of turbulent atmosphere, the index fluctuations will induce phase errors in the pupil of an imaging system. Let  $H(\mathbf{u})$  represent the generalized pupil function:

$$H(\mathbf{u}) = |H(\mathbf{u})| \exp\{i\phi(\mathbf{u})\} , \quad (4-6)$$

where  $|H(\mathbf{u})|$  is the transmittance function (typically a binary aperture function) and  $\phi(\mathbf{u})$  is the phase-aberration function. We are using  $\mathbf{u}$  to represent a spatial-frequency vector that is related to a spatial vector  $\mathbf{r}$  in the physical pupil of the system by

$$\mathbf{r} = \lambda R \mathbf{u} , \quad (4-7)$$

where  $\lambda$  is the wavelength and  $R$  is the range to the target (source of the spherical wave). The phase-aberration function at each spatial frequency is the sum of a great number of independent random variables due to the path integration [4.1]. The central limit theorem implies that  $\phi(\mathbf{u})$  will be a Gaussian random process.

The Optical Transfer Function (OTF) is used to characterize imaging performance for incoherent imaging systems. The OTF is computed by taking the spatial autocorrelation

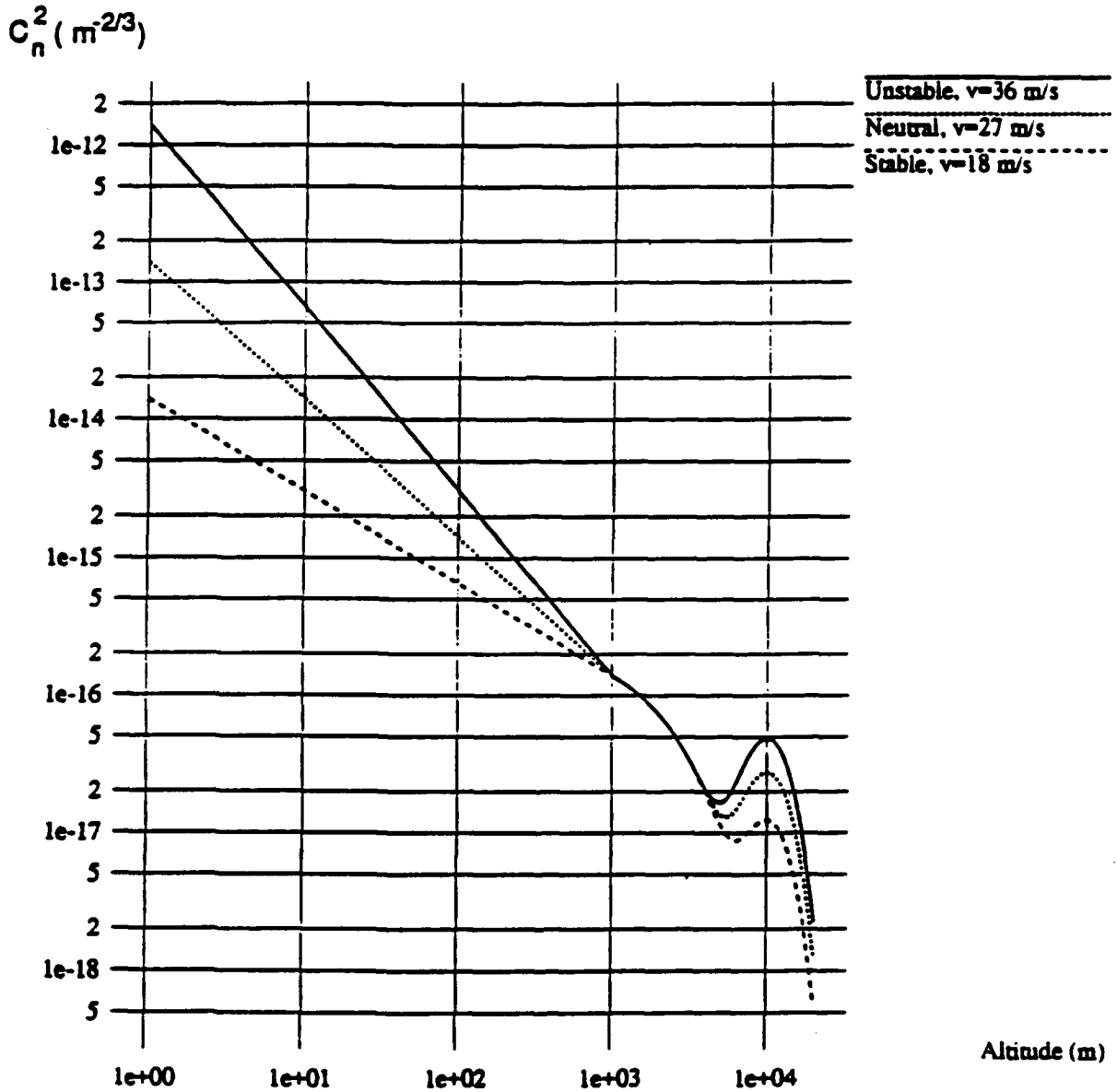


Figure 4-1: Index Structure Parameter Profiles Using Extended Hufnagel Model. The index structure parameter,  $C_n^2$ , is plotted as a function of altitude for stable (desirable), neutral, and unstable (undesirable) conditions.

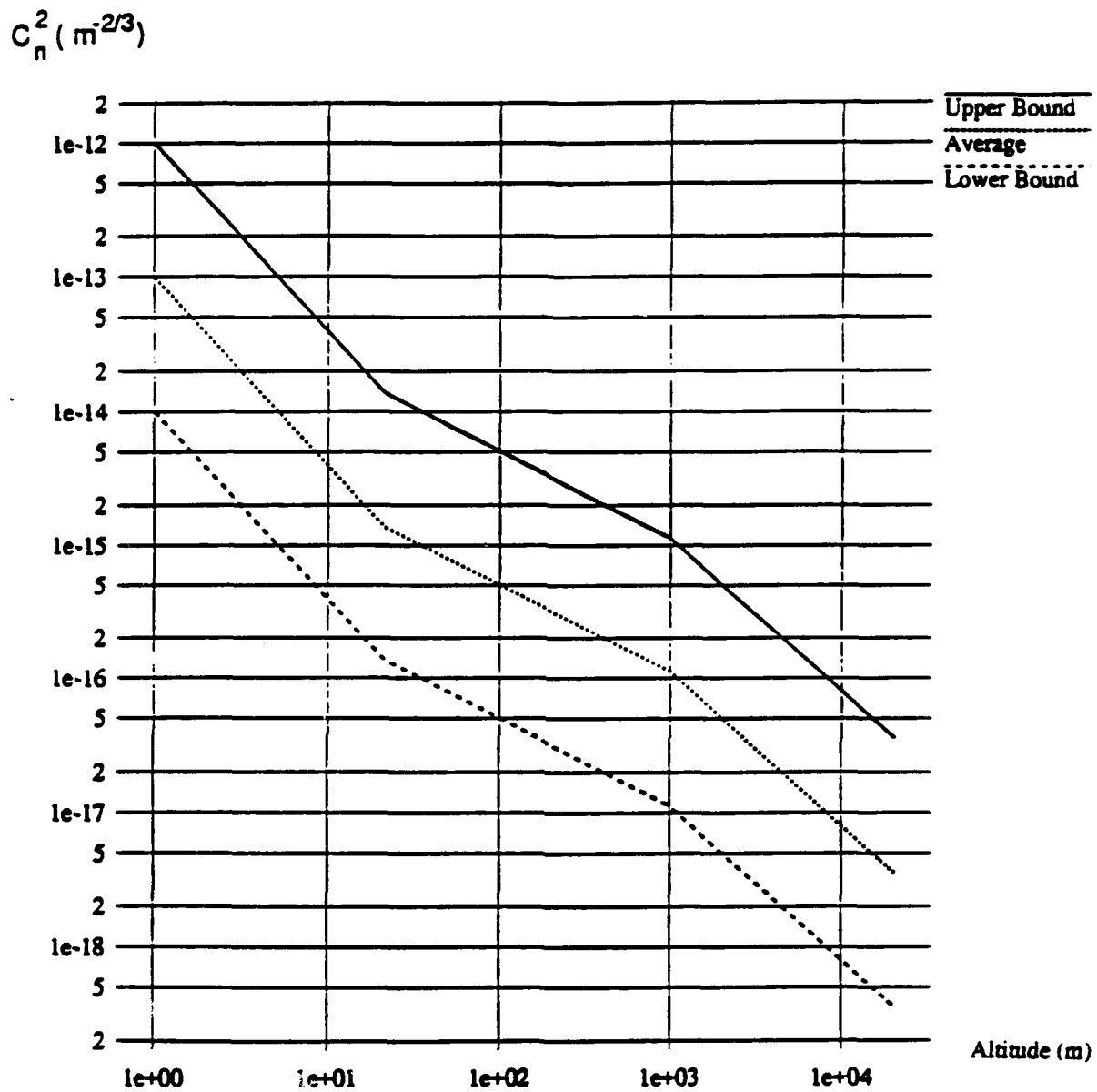


Figure 4-2: Index Structure Parameter Profiles Using Empirical Model. A lower bound (optimistic), average, and upper bound (pessimistic) for the index structure parameter,  $C_n^2$ , is plotted as a function of altitude.

of the generalized pupil function.

$$T(\mathbf{u}) = \int H(\mathbf{u}')H^*(\mathbf{u}' - \mathbf{u}) d\mathbf{u}' . \quad (4-8)$$

$$(4-9)$$

In many imaging applications, exposures times are long relative to the evolution of the atmosphere. In this case it is the time-averaged OTF that determines imaging performance. Under the assumption that temporal and ensemble averages yield the same result, the long-exposure OTF is given by

$$\langle T(\mathbf{u}) \rangle = \left\langle \int H(\mathbf{u}')H^*(\mathbf{u}' - \mathbf{u}) d\mathbf{u}' \right\rangle \quad (4-10)$$

$$= \int |H(\mathbf{u}')||H^*(\mathbf{u}' - \mathbf{u})| \langle \exp\{i[\phi(\mathbf{u}') - \phi(\mathbf{u}' - \mathbf{u})]\} \rangle d\mathbf{u}' . \quad (4-11)$$

Notice that the transmittance function is fixed in time and that the ensemble average is over the phase contribution of the generalized pupil function. We now isolate our attention on the expression in the angle brackets. This expression may be regarded as the characteristic function of  $\phi(\mathbf{u}') - \phi(\mathbf{u}' - \mathbf{u})$  evaluated at unit frequency. Since  $\phi(\mathbf{u})$  is a Gaussian random process,  $\phi(\mathbf{u}') - \phi(\mathbf{u}' - \mathbf{u})$  will be a zero-mean Gaussian random process with variance

$$\sigma^2 = \langle |\phi(\mathbf{u}') - \phi(\mathbf{u}' - \mathbf{u})|^2 \rangle . \quad (4-12)$$

It is well known that the characteristic function of a zero-mean Gaussian random variable with a probability density function

$$p_Z(z) = \frac{1}{\sigma\sqrt{2\pi}} \exp\{-z^2/2\sigma^2\} \quad (4-13)$$

will have a characteristic function

$$\int p_Z(z) \exp\{i\omega z\} dz = \exp\{-\sigma^2\omega^2/2\} . \quad (4-14)$$

Therefore

$$\langle \exp\{i[\phi(\mathbf{u}') - \phi(\mathbf{u}' - \mathbf{u})]\} \rangle = \exp\left\{-\frac{1}{2}\langle |\phi(\mathbf{u}') - \phi(\mathbf{u}' - \mathbf{u})|^2 \rangle\right\} \quad (4-15)$$

$$= \exp\left\{-\frac{1}{2}D_\phi(-\mathbf{u})\right\} . \quad (4-16)$$

Thus the expression in angle brackets in Eq. (4-11) has the form of an exponential function with a phase structure function as the argument. Since this expression is not a function of  $\mathbf{u}'$ , it can come out of the integral in Eq. (4-11).

$$\langle T(\mathbf{u}) \rangle = \exp \left\{ -\frac{1}{2} D_\phi(-\mathbf{u}) \right\} \int |H(\mathbf{u}')| |H^*(\mathbf{u}' - \mathbf{u})| d\mathbf{u}' \quad (4-17)$$

$$= \exp \left\{ -\frac{1}{2} D_\phi(-\mathbf{u}) \right\} T_d(\mathbf{u}), \quad (4-18)$$

where  $T_d(\mathbf{u})$  is recognized as the diffraction-limited OTF.

The statistics of phase and amplitude of a spherical wave propagating through turbulence has been investigated by numerous researchers. The most influential work on this subject was performed by Tatarski. Tatarski derived the phase structure function using the Rytov approximation [4.5]

$$D_\phi(r) = 2.91 \left( \frac{2\pi}{\lambda} \right)^2 r^{5/3} \int_0^R C_n^2(z) [1 - (z/R)]^{5/3} dz, \quad (4-19)$$

where  $R$  is the range to the target,  $z$  is the path-integration variable, and the path integration runs from the pupil to the target. A heuristic derivation for the plane-wave equivalent of Eq. (4-19) is given by [4.1]. Recall that the phase structure function is defined as the mean-square phase error between two points separated by a distance  $r$  in the pupil. Notice that the path integral in Eq. (4-19) is a weighted integral of the index structure parameter in which the weight is strongest near the sensor. The interpretation is that turbulence near the sensor contributes more to the phase errors in the pupil than does comparable turbulence near the target.

Fried has defined the correlation diameter (or seeing parameter) to be

$$r_o \equiv \left\{ \left( \frac{2.91}{6.88} \right) \left( \frac{2\pi}{\lambda} \right)^2 \int_0^R C_n^2(z) [1 - (z/R)]^{5/3} dz \right\}^{-3/5}. \quad (4-20)$$

This definition immediately simplifies the expression for the phase structure function.

$$D_\phi(r) = 6.88 \left( \frac{r}{r_o} \right)^{5/3}. \quad (4-21)$$

In addition to simplifying the expression for the phase structure function,  $r_o$  serves as a fundamental parameter with a simple physical interpretation that characterizes the induced phase aberrations. This interpretation utilizes the resolving power of an incoherent imaging

system as a figure of merit for image quality. The resolving power is defined as the integral over spatial frequency of the optical transfer function [4.1].

$$\mathcal{R}_T \equiv \int T(u) du . \quad (4-22)$$

Recall that the incoherent point-spread function (PSF) is just the Fourier transform of the OTF (normalized). Therefore, the resolving power is also the value of the PSF at the origin (by the central ordinate theorem). Because long-exposure OTFs are real-valued (see Eqs. (4-11) and (4-21), the value of the PSF at the origin is also the maximum value of the PSF. Thus the resolving power is closely related to the Strehl metric for image quality [4.6].

It is interesting to observe the behavior of the resolving power as the diameter of the system aperture function increases. Of course in the absence of turbulence (diffraction-limited case), the resolving power will increase in concert with an increase in aperture diameter. However, in the presence of turbulence, the resolving power is seen to approach an asymptotic limit as the aperture diameter increases. Thus for very large diameter systems, the resolving power will be limited by turbulence. This is depicted in Figure (4-3). The correlation diameter is defined implicitly as the diameter that a diffraction-limited system must assume in order to achieve the same resolving power as a turbulence-limited system. Formally,  $r_o$  must satisfy

$$\int T_d^{r_o}(u) du = \int \langle T^\infty(u) \rangle du \quad (4-23)$$

where  $T^r(u)$  represents an OTF with diameter  $r$ . The derivation of the explicit expression for  $r_o$  (Eq. (4-20)) from this implicit definition is provided by [4.1].

Occasionally investigators have held the misconception that there is little value in designing a telescope aperture to be greater than the value of  $r_o$ . Careful study of Figure (4-3) will reveal that the resolving power will continue to increase (improve) for apertures of diameter 3 to 5 times  $r_o$ . This is an important point for the long-range laser imaging system design, to which we will return later. Clearly, when the diameter reaches  $10r_o$ , there is little to be gained with regard to resolving power by increasing the aperture size.

We now give values for  $r_o$  computed for the long-range laser-imaging geometry. The baseline geometry locates the sensor platform at an altitude of 13.1 Km and the target at ground level, with the slant range to the target being  $R = 100 Km$ . We assume that the wavelength of the radiation is  $\lambda = 1.0 \mu m$ . From Eq. (4-20) we see that  $r_o$  scales with wavelength according to  $\lambda^{6/5}$ . Thus, it is easy to scale a computed value of  $r_o$  according to

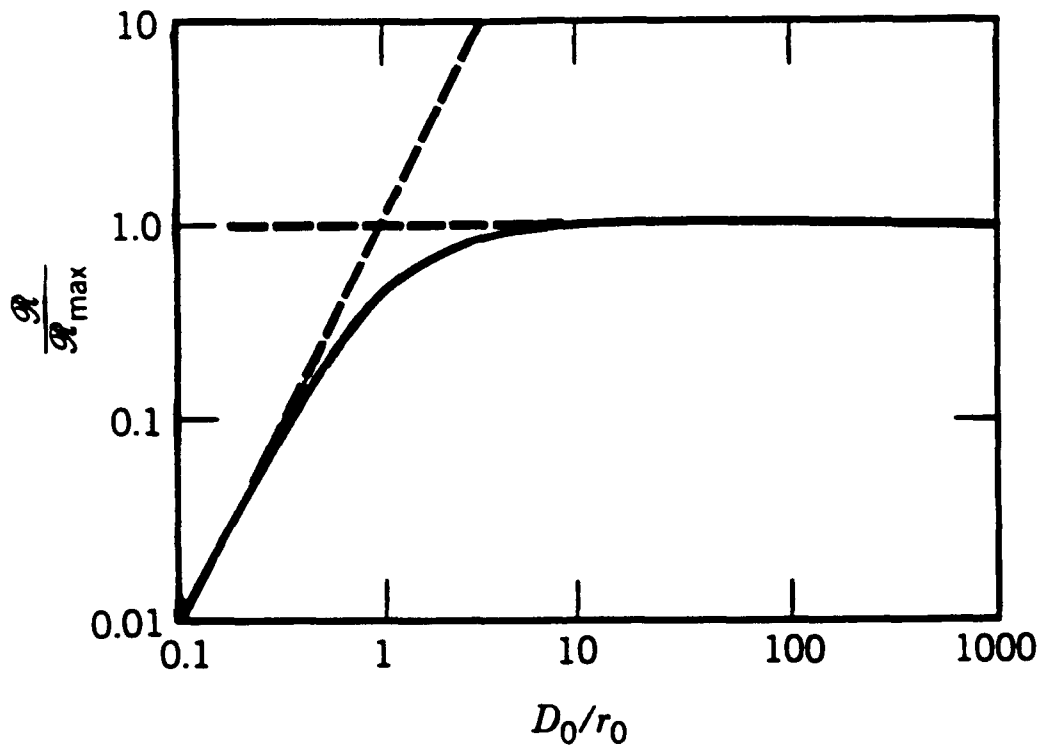


Figure 4-3: Resolving Power as a Function of Aperture Diameter. The resolving power of an incoherent imaging system (normalized by the maximum resolving power,  $\mathcal{R}_{max}$ ) is plotted as a function of the aperture diameter (normalized by the correlation diameter,  $r_o$ ). The horizontal asymptote indicates the resolving power saturates at  $\mathcal{R}_{max}$ . The slanted asymptote indicates the resolving power that would be achieved in the absence of turbulence (diffraction-limited case). The value of  $r_o$  is defined by the intersection of these two asymptotes. (Graph reproduced from [4.7], originally given by [4.8]).

Model	$r_0$ (m)	$M(r = .2 m)$
Hufnagel stable	0.29	.16
Hufnagel neutral	0.20	.032
Hufnagel unstable	0.15	.004
empirical stable	1.31	.86
empirical neutral	0.33	.22
empirical unstable	0.08	.1 e-6

Table 4-1: Computed values of  $r_0$  and OTF modulation at  $r = .2 m$

the desired wavelength. From Eq. (4-20) we also see that the computation of  $r_0$  involves a path integral and therefore requires a model for the structure parameter profile. Table 4-1 gives the computed values of  $r_0$  for each of the 6 structure-parameter models discussed in Section 4.3. Notice that these values are somewhat better than would be expected in astronomical settings. This is because the platform is at an altitude where the turbulence is considerably reduced from that at the ground. The weighting in the integral (Eq. (4-20)) that emphasizes turbulence proximate to the sensor and deemphasizes turbulence near the target yields these favorable values. The table entries range from the most pessimistic case of  $r_0 = 8 \text{ cm}$  to the most optimistic case of  $r_0 = 1.31 \text{ m}$ , suggesting that considerable variability can be expected in  $r_0$ . We believe that the LRLI system should be designed to accommodate  $r_0$  values that vary between 10 and 40  $\text{cm}$ .

Recall from Eq. (4-11) that the turbulence has the effect of modulating (reducing) the diffraction-limited OTF. This modulation has the form

$$M(r) = \exp \left\{ -\frac{1}{2} D_\phi(r) \right\} \quad (4-24)$$

$$= \exp \left\{ -3.44 \left( \frac{r}{r_0} \right)^{5/3} \right\} \quad (4-25)$$

where we have also used Eq. (4-21). Table 4-1 also gives the OTF modulation for points separated in the pupil by  $r = 0.2 \text{ m}$  for each of the 6 atmospheric models. An early LRLI system concept involved an aperture with a 0.3  $\text{m}$  diameter. The evaluation of the modulation at  $r = 0.2 \text{ m}$  was intended to suggest the effect of turbulence on the higher spatial frequencies.

## 4.5 Adaptive Correction of Phase Errors

One strategy for dealing with phase errors induced by atmospheric turbulence is to sense these errors and adaptively correct for them with a deformable mirror in real time. The goal would be to achieve resolutions approaching the diffraction limit of the telescope. However, adaptive-optics systems are expensive and impose significant engineering challenges. In this section, we investigate the utility of an adaptive-optics system in the LRLI scenario. Under the assumption that ideal wavefront sensing and adaptive correction can be accomplished at very high temporal bandwidth (essentially instantaneously). Under these assumptions, adaptive correction over the field-of-view will be limited by anisoplanatic effects.

Figure 4-4 depicts the imaging geometry for the LRLI sensor. Notice that spherical waves launched from different points in the field-of-view will pass through different atmospheric turbulence over much of their paths. This is particularly true at low altitudes (near the scene) where the turbulence is strongest. This effect, known as anisoplanatism, implies that the short-exposure PSF (short relative to the evolution of the atmosphere) will vary with position in the field. Therefore, an imaging system that collects short-exposure imagery will be space-variant. By contrast, when the system collects long-exposure imagery, it will be space-invariant.

Consider a beacon in the center of the field of view that is used for wavefront sensing with subsequent phase-error correction with a deformable mirror. An adaptive-optics system is designed to correct phase aberrations as they evolve so that the imagery close to the beacon will be diffraction-limited even for long-exposure imagery. However, the phase-error correction will be imperfect for points in the field-of-view that are somewhat displaced from the beacon location and the long-exposure imagery will not be diffraction-limited. In order to quantify this behavior, Fried has derived an expression for anisoplanatism-induced mean-square phase error in an adaptively corrected system [4.9]:

$$\begin{aligned}
 S(\mathbf{r}, \boldsymbol{\alpha}) = & 2.905 \left(\frac{2\pi}{\lambda}\right)^2 \int_0^R C_n^2(z) \left( \{r[1 - (z/R)]\}^{5/3} + (\alpha z)^{5/3} \right. \\
 & - \frac{1}{2} |\{r[1 - (z/R)]\}^2 + 2r\alpha z[1 - (z/R)] + (\alpha z)^2|^{5/6} \\
 & \left. - \frac{1}{2} |\{r[1 - (z/R)]\}^2 - 2r\alpha z[1 - (z/R)] + (\alpha z)^2|^{5/6} \right) dz \quad (4-26)
 \end{aligned}$$

where  $\boldsymbol{\alpha}$  is a field-angle vector relative to the beacon and

$$c \equiv \mathbf{r} \cdot \boldsymbol{\alpha} / (r\alpha) . \quad (4-27)$$

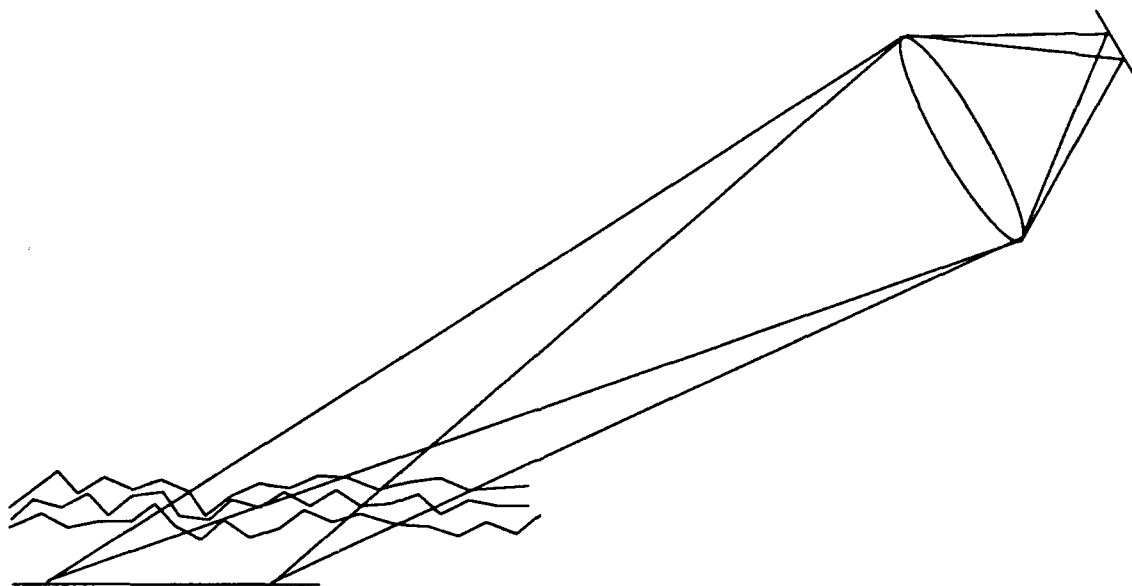


Figure 4-4: Anisoplanatic Imaging. Induced phase errors will be different for different points in the field-of-view for the LRLI geometry.

The function  $S(\mathbf{r}, \alpha)$  is interpreted as the mean-square phase error between points in the pupil separated by  $\mathbf{r}$  for a point in the field-of-view at field-angle  $\alpha$ . Equation (4-26) applies to a system with ideal phase correction for waves generated at the beacon. It is straightforward to confirm that  $S(\mathbf{r}, \alpha) = 0$  when  $\alpha = 0$ , as expected.

Fried also quotes a result that shows the effect of the anisoplanatism-induced mean-square phase error on the long-exposure OTF when adaptively correcting phase errors at the beacon [4.9]

$$\langle T(\mathbf{u}, \alpha) \rangle \approx T_d(\mathbf{u}) \exp\{-S(R\lambda\mathbf{u}, \alpha)\}, \quad (4-28)$$

where the approximation is due to the assumption that scintillation effects are negligible. Notice that the long-exposure OTF is a function of spatial-frequency *and* field position for a system with adaptive correction. The long-exposure OTF is seen to be the diffraction-limited OTF modulated by an exponential whose argument is the negative of the anisoplanatism-induced mean-square phase error. The function  $S(\mathbf{r}, \alpha)$  therefore plays a role in the adaptive case similar to that of the phase structure function in the nonadaptive case.

A plot of the anisoplanatism-induced root-mean square (RMS) phase error ( $S^{1/2}$ ) for points separated by  $.2m$  in the pupil as a function of field position on the ground ( $R\alpha$ ) is given in Figure 4-5. This plot was computed by repeatedly evaluating Eq. (4-26) for the LRLI geometry and the Hufnagel neutral  $C_n^2$  profile. Signal-level considerations suggest that the instantaneous field-of-view may be approximately  $100m \times 100m$  in cross-range coordinates. In this plot we assume that the beacon is at the origin and we have plotted the RMS phase error as a function of field position out to  $50m$ . We have also plotted the particular case for which the field angle vector,  $\alpha$ , is perpendicular to the separation vector in the pupil,  $\mathbf{r}$ . This plot shows that the RMS phase increases rapidly as the field position moves away from the beacon. The RMS phase error is nearly a quarter of a wave (strongly aberrated) at only a meter or two from the beacon. This suggests that the anisoplanatism is severe for the LRLI geometry and that conventional adaptive optics could only correct phase errors over a very small patch around the beacon.

The isoplanatic angle has been defined by Fried to be

$$\alpha_o \equiv \left[ 2.91 \left( \frac{2\pi}{\lambda} \right)^2 \int_0^R C_n^2(z) z^{5/3} dz \right]^{-3/5}. \quad (4-29)$$

Notice that this expression resembles the definition of  $r_o$  (Eq. (4-20)), although there is a

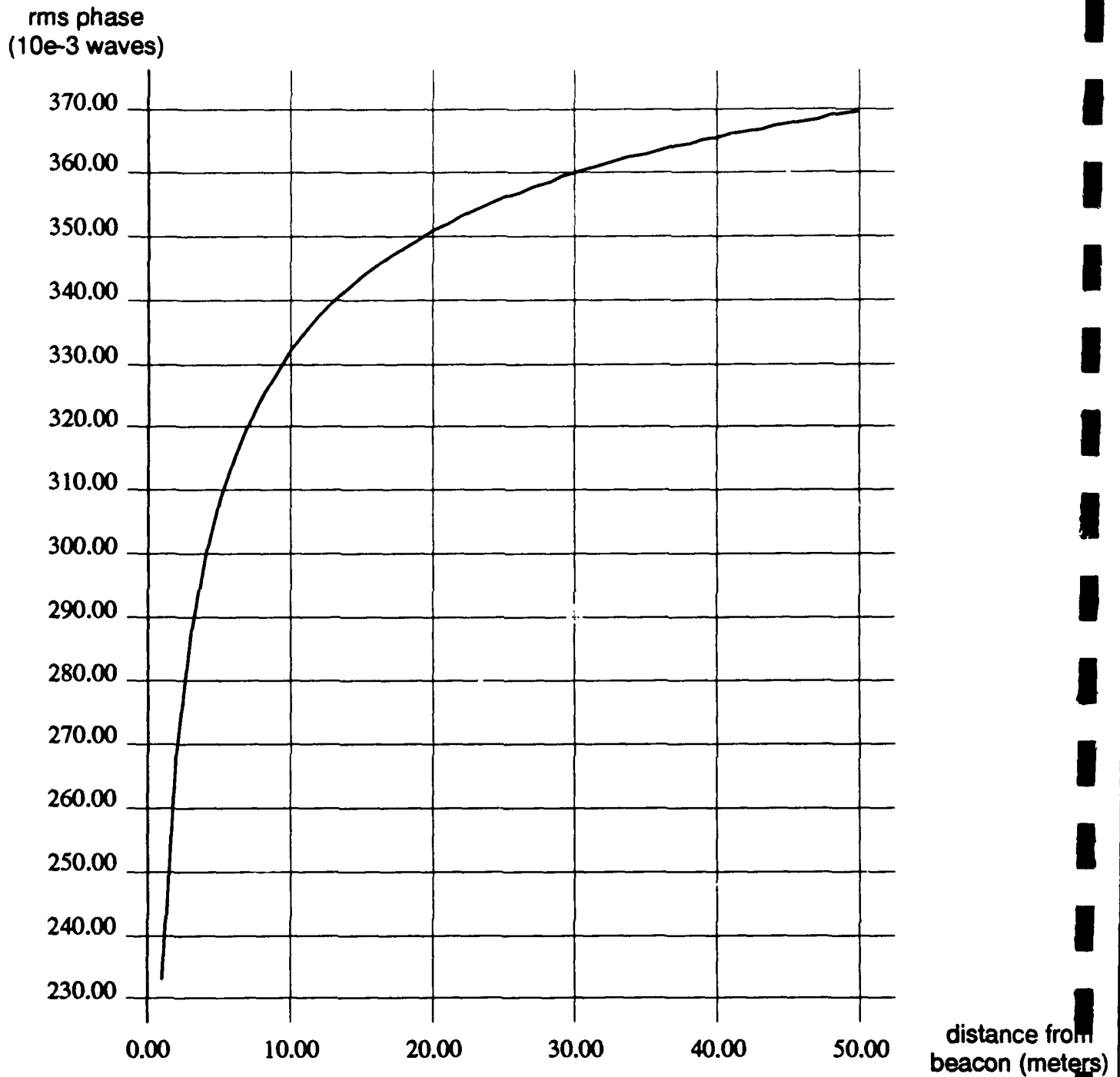


Figure 4-5: RMS Phase Error as a Function of Field Position. The RMS phase error in waves between 2 points in the pupil separated by .2m is given as a function of field position in cross-range coordinates.

different scale factor and the path integral emphasizes turbulence near the target. In order to interpret the meaning of the anisoplanatic angle it is useful to consider the anisoplanatism induced mean-square phase error in two important limiting cases.

$$\lim_{r/\alpha \rightarrow \infty} S(\mathbf{r}, \alpha) = \left( \frac{\alpha}{\alpha_0} \right)^{5/3} \quad (4-30)$$

$$\lim_{r/\alpha \rightarrow 0} S(\mathbf{r}, \alpha) = 6.88 \left( \frac{r}{r_0} \right)^{5/3} \quad (4-31)$$

These expressions readily derive from Eq. (4-26). The first case (Eq. (4-30)) approximately holds when examining field positions close to the beacon and points in the pupil with significant separation. In this limit we see that the expression for  $S(\mathbf{r}, \alpha)$  has a particularly simple form given the definition of the isoplanatic angle. Notice that the OTF modulation (Eq. (4-28)) is relatively minor for field angles less than  $\alpha_0$  whereas they are rather severe for field angles greater than  $\alpha_0$ . The second case approximates the behavior for field positions far from the beacon. Notice that the OTF modulation implied by this expression is very similar to that which occurs when there is no adaptive correction (Eq. (4-25)). However, in the case of adaptive correction the argument of the exponential is exactly twice that encountered in the nonadaptive case. This can be understood by realizing that when two field points are well separated, the induced phase errors will be uncorrelated. Adaptive correction of the phase errors for one of the points (the beacon) will then add deformable-mirror phase errors to the turbulence-induced phase errors associated with the other point. Since these phase errors are zero-mean Gaussian, the mean-square phase errors (variances) will add and the phase structure function will be exactly twice that of the uncorrected case. Thus when an image point is well separated from the beacon, adaptive correction actually degrades performance and has the net effect of doubling the strength of the turbulence.

Equation (4-29) was used to compute the isoplanatic angle for the LRLI geometry for each of the 6  $C_n^2$  profiles discussed in Section 4.3. Table 4-2 presents these computed isoplanatic angles scaled by the range  $R$  to give a cross-range isoplanatic patch size at the target. Notice that under each of the turbulence models the isoplanatic patch size is extremely small relative to the anticipated size of the field-of-view. These values are consistent with Table 4-1 and the observation that conventional adaptive optics may only be able to correct phase errors over a very small patch about the beacon.

Table 4-2 also gives the OTF modulation for points in the pupil separated by  $r = .2m$  in both the uncompensated and compensated cases. The uncompensated modulation,

Model	$r_o (m)$	$R\alpha_o (m)$	$M_u$	$M_c(R\alpha = 50 m)$	$M_c(R\alpha = \infty)$
Hufnagel stable	0.29	.02	.16	.056	.024
Hufnagel neutral	0.20	.01	.032	.005	.001
Hufnagel unstable	0.15	.003	.004	.0001	.14 e-5
empirical stable	1.31	.05	.86	.78	.741
empirical neutral	0.33	.013	.22	.09	.051
empirical unstable	0.08	.003	.1 e-6	.3 e-10	.17 e-14

Table 4-2: Computed Values of  $r_o$ ,  $R\alpha_o$ , and Various OTF Modulations.  $M_u$  represents modulation for points in the pupil separated by  $r = .2m$  in the uncompensated case.  $M_c$  represents modulation for the same pupil separation in the compensated case. Compensated modulation is given for field points 50  $m$  from the beacon and infinitely far from the beacon.

$M_u$ , is computed using Eq. (4-25) and is uniform over the field-of-view. The compensated modulation follows from Eq. (4-28),

$$M_c(\mathbf{r}, \alpha) = \exp\{-S(\mathbf{r}, \alpha)\} , \quad (4-32)$$

and will vary with field position. Table 4-2 gives  $M_c$  for  $R\alpha = 50 m$  (at the edge of the anticipated field-of-view) using Eq. (4-26) and for  $R\alpha = \infty$  using Eq. (4-31) to give the asymptotic behavior. It is clear that the compensated modulation is significantly worse (smaller) at the edge of the field-of-view than is the uncompensated modulation. Thus for points at the edge of the field-of-view, compensation actually degrades resolution.

The small isoplanatic patch sizes suggest that most of the field-of-view would suffer from adaptive-optics induced degradation. However, isoplanatic angle is defined by its asymptotic role which does not strictly apply with finite apertures and displacements from the beacon. One could define a field patch outside of which compensation degrades resolution for a particular imaging geometry. The boundary of such a patch, consisting of the locus of points,  $\{\alpha_c\}$ , could be implicitly defined using a resolving-power criterion as follows

$$\int T_d(\mathbf{u}) \exp\{-S(\mathbf{u}, \alpha_c)\} d\mathbf{u} = \int T_d(\mathbf{u}) \exp\{-D_\phi(\mathbf{u})/2\} d\mathbf{u} . \quad (4-33)$$

Such a boundary would probably have to be located numerically.

Another problem that would be encountered with the use of adaptive optics is the demanding temporal bandwidths that would need to be achieved in the long-range laser

imaging scenario. The Greenwood frequency has been used as a measure of required bandwidths for adaptive-optics systems. The Greenwood frequency is given by [4.10]

$$f_g = \left\{ 0.102 \left( \frac{2\pi}{\lambda} \right)^2 \int_0^R C_n^2(z) v^{5/3}(z) dz \right\}^{3/5}, \quad (4-34)$$

where  $v(z)$  is the transverse wind speed along the path of propagation. A first-order estimate of the Greenwood frequency can be computed by assuming that the atmosphere is frozen and that the effective wind speed is due entirely to the platform motion. We take the platform speed to be 450 *knots* or 833 *Km/hr* (518 *mi/hr*). Therefore, the effective wind speed at the platform is

$$v(0) = 833 \text{ Km/hr}, \quad (4-35)$$

and the effective wind speed along the path will be

$$v(z) = (1 - z/R)v(0). \quad (4-36)$$

Substituting Eq. (4-36) into Eq. (4-34) we get

$$f_g = \left\{ 0.102 \left( \frac{2\pi}{\lambda} \right)^2 \int_0^R C_n^2(z) [(1 - z/R)v(0)]^{5/3} dz \right\}^{3/5} \quad (4-37)$$

$$= v(0) \left\{ 0.102 \left( \frac{2\pi}{\lambda} \right)^2 \int_0^R C_n^2(z) (1 - z/R)^{5/3} dz \right\}^{3/5}. \quad (4-38)$$

This expression is reminiscent of the expression for  $r_o$ , Eq. (4-20). By appropriate algebraic manipulation, we can write the Greenwood frequency in terms of the correlation diameter:

$$f_g = v(0) [0.241 r_o^{-5/3}]^{3/5} \quad (4-39)$$

$$= .426 v(0) r_o^{-1}. \quad (4-40)$$

Using the correlation diameters computed for the long-range laser imaging scenario we can quickly predict the Greenwood frequency. These are given in Table 4-3. These calculations suggest that an adaptive-optics system would have to accommodate a Greenwood frequency of perhaps 500 *Hz* or more. Note that in practice the closed-loop servo bandwidth in an adaptive-optics system needs to be several times the Greenwood frequency [4.10]. Therefore,

Model	$r_0$ (m)	$f_g$ (Hz)
Hufnagel stable	0.29	340
Hufnagel neutral	0.20	493
Hufnagel unstable	0.15	657
empirical stable	1.31	75
empirical neutral	0.33	299
empirical unstable	0.08	1233

Table 4-3: Computed values of  $r_0$  and Greenwood frequency,  $f_g$ .

for this particular imaging scenario, the use of adaptive optics is very challenging with regards to temporal bandwidths alone.

#### 4.6 Induced Amplitude Errors

The theory of induced phase errors as presented thus far was derived under the near-field turbulence approximation. This approximation implies that errors in the wavefront at the pupil manifest themselves solely as phase errors. Such a model is often appropriate for astronomical imaging, where the turbulence is located proximate to the entrance pupil. In the LRLI scenario, however, turbulence is distributed along an extended optical path and the strongest turbulence is remote to the entrance pupil. In this case, wavefront errors at the entrance pupil will be manifest as both phase and amplitude errors. The variation in amplitude resulting from atmospheric turbulence is referred to as scintillation. Because of the LRLI geometry, the effects of scintillation needs to be considered.

When the theory of induced phase errors is generalized to accommodate amplitude errors [4.7], the long-exposure OTF takes on the form

$$\langle T(\mathbf{u}) \rangle = \exp \left\{ -\frac{1}{2} D_w(-\mathbf{u}) \right\} T_d(\mathbf{u}), \quad (4-41)$$

where  $T_d(\mathbf{u})$  is the diffraction-limited OTF and  $D_w(\mathbf{u})$  is the *wave* structure function. The wave structure function is defined as

$$D_w(\mathbf{u}) = D_\phi(\mathbf{u}) + D_\chi(\mathbf{u}), \quad (4-42)$$

where  $\chi$  is the log of the amplitude of the wavefront at the pupil and  $D_\chi(\mathbf{u})$  is the log-

amplitude structure function. Surprisingly, the wave structure function, as derived by Tatarski using the Rytov approximation [4.5,4.7], has the same form as the near-field phase structure function

$$D_w(r) = 2.91 \left( \frac{2\pi}{\lambda} \right)^2 r^{5/3} \int_0^R C_n^2(z) [1 - (z/R)]^{5/3} dz, \quad (4-43)$$

where we have maintained the convention that the path integration runs from the pupil to the target. Since the wave structure function has the same form as the near-field phase structure function, the values of  $r_o$  presented in Table 4-1 actually account for both phase and amplitude errors. In fact, the Rytov theory predicts that as the turbulence increases in strength, amplitude variations will also increase without bound. However, measurements demonstrate that amplitude variations saturate [4.11]. Therefore, our computed values of  $r_o$  may even be slightly pessimistic.

#### 4.7 Aero-Optical Effects

To this point, we have considered only aberrations that arise from naturally occurring index-of-refraction variations in the atmosphere. Another source of optical aberrations is the index variations arising from platform aerodynamics. The subject of aero-optical effects deals with many types of airflow disturbances, including laminar flow, turbulent boundary layers, shear layers, inviscid flow, and shock waves [4.12]. It is beyond the scope of this study to investigate the various telescope mounting/window strategies and the resulting atmospheric disturbances that can arise in each case. Instead, we consider one possible engineering solution and show that the aberrations that are produced are rather benign.

One attractive design is to use a flush material window of high quality. Since the wavelength is nominally  $1 \mu m$ , thermal emission from the window material should not be significant. The flow field in this case will be an attached turbulent boundary layer. The predicted wavefront variance is given by [4.12]

$$\sigma^2 = 2G^2 \int_0^L \langle \rho'^2 \rangle l_z dz, \quad (4-44)$$

where  $G$  is the Gladstone-Dale parameter ( $0.22 \text{ cm}^3/\text{gm}$ ),  $L$  is the length of the disturbance along the optical axis,  $\rho'$  is the flow fields' fluctuating density, and  $l_z$  is the correlation length in the direction of the optical axis. The boundary-layer thickness grows with the distance

along the fuselage (streamwise). The thickness obeys a power law [4.12],

$$L \approx .024 x^{.8} , \quad (4-45)$$

where  $x$  is the distance from the nose of the aircraft to the point downstream being considered. The platform speed is taken to be 450 *knots* or approximately Mach 0.7. For fully developed subsonic turbulent boundary layers the correlation length is approximately 10% of the boundary-layer thickness [4.12],

$$l_z = 0.1 L . \quad (4-46)$$

An engineering expression for the density at the surface of the aircraft is [4.12]

$$\rho_s = \rho_o \left[ 1 + r \left( \frac{\gamma - 1}{2} \right) M^2 \right]^{-1} , \quad (4-47)$$

where

$$\rho_o = \text{free-stream density} \quad (4-48)$$

$$r = \text{recovery factor} \quad (4-49)$$

$$\gamma = \text{adiabatic index} \quad (4-50)$$

$$M = \text{Mach number} \quad (4-51)$$

We are now in a position to compute the expected phase variance for a specific situation. This calculation closely parallels an example calculation found in [4.12]. We assume that the window is located at  $x = 10 m$  from the nose of the aircraft. This implies that  $L = 15 cm$  and  $l_z = 1.5 cm$ . At an altitude of 12 *Km* the free stream-density will be  $\rho_o = 3.1 e-4 g/cm^3$ . The recovery factor for the case of turbulent mixing is  $r = 0.89$  and the adiabatic index for air is  $\gamma = 1.4$ . From Eq.(4-47), the density at the aircraft surface is computed to be  $\rho_s = 2.85 e-4 g/cm^3$ . The variance in the density may be approximated as 10% of the difference between the density at the aircraft surface and the free-stream density:

$$\rho' = 0.1 (\rho_o - \rho_s) \quad (4-52)$$

$$= 2.5 e-6 g/cm^3 . \quad (4-53)$$

Using these values in Eq. (4-44) we can estimate the root-mean-square wavefront error to be

$$\sigma = G\rho'(2l_z L)^{1/2} \quad (4-54)$$

$$= .037 \mu m . \quad (4-55)$$

For  $\lambda = 1 \mu m$ , this means that there will only be less than 4/100 wave rms phase error, which is a very small amount of phase aberrations that will have little effect on image quality.

From this first-order calculation, we conclude that the aero-optical effects are probably manageable. Obviously, the design of the window and its location in the aircraft are important issues that need to be studied in more depth. If an optical turret is needed to increase the range of pointing then computer simulation would be required to model the protuberance and the resulting inviscid airflow. Inviscid airflow tends to be stable. Such an aberration could be corrected with a low-bandwidth adaptive system.

## 4.8 Conclusions

We have shown that the effects of anisoplanatism are severe in the LRLI geometry. In addition, temporal bandwidths required for adaptive optics would be an engineering challenge. As a consequence, we judge that conventional adaptive optics (utilizing a single deformable mirror in the pupil plane) are of limited utility for this sensor. By contrast, uncompensated seeing has been shown to be rather favorable for a wide range of turbulence profiles. It appears that aero-optical effects will be manageable with such an approach. We believe that the LRLI system should be designed to accommodate  $r_o$  values that vary between 10 and 40 *cm* for  $\lambda = 1 \mu m$ . Given an actual aperture diameter somewhat larger than  $r_o$  (perhaps 1 *m*), resolutions close to  $R\lambda/r_o$  can be achieved. In the LRLI geometry this implies cross-range resolutions ranging from about .25 to 1.0 *m*, which is sufficient for LRLI missions. The likely elimination of the need for an adaptive optics system means a significant savings in cost and complexity for the LRLI concept.

## 4.9 References

- [4.1] F. Roddier, "The effects of atmospheric turbulence in optical astronomy," in *Progress in Optics XIX*, ed. E. Wolf (North Holland, 1981), Ch. 5.
- [4.2] *The Infrared Handbook*, eds. G.J. Zissis and W.L. Wolfe (Office of Naval Research, Washington, 1978), Chapter 6.
- [4.3] T. Barletti, et al., "Mean vertical profile of atmospheric turbulence relevant for astronomical seeing," *J. Op. Soc. Am.* **66**, 1380 (1976).
- [4.4] A.E. Gur'yanov, "Astronomical image quality and the vertical distribution of turbulent optical interference in the night atmosphere," *Sov. Astron.* **28**, 343-350 (1984).
- [4.5] V.I. Tatarski, *Wave Propagation in a Turbulent Medium* (McGraw Hill, New York, 1961).
- [4.6] M. Born and E. Wolf, *Principles of Optics* (Pergamon Press, New York, 1959).
- [4.7] J.W. Goodman, *Statistical Optics* (Wiley, New York, 1985).
- [4.8] D.L. Fried, "Optical resolution through a randomly inhomogeneous medium for very long and very short exposures," *J. Opt. Soc. Am.* **56**, 1372-1379 (1966).
- [4.9] D.L. Fried, "Anisoplanatism in adaptive optics," *J. Opt. Soc. Am.* **72**, 52-61 (1982).
- [4.10] R.K. Tyson and P.B. Ulrich, "Adaptive optics," in *The Infrared & Electro-Optical Systems Handbook, Volume 8: Emerging Systems and Technologies*, S.R. Robinson, Ed. (SPIE Optical Engineering Press, Bellingham, Washington, 1993).
- [4.11] R.R. Beland, "Propagation through atmospheric optical turbulence," in *The Infrared & Electro-Optical Systems Handbook, Volume 2: Atmospheric Propagation of Radiation*, F.G. Smith, ed. (SPIE Optical Engineering Press, Bellingham, Washington, 1993).
- [4.12] K.G. Gilbert, L.J. Otten, and W.C. Rose, "Aerodynamic effects," in *The Infrared & Electro-Optical Systems Handbook, Volume 2: Atmospheric Propagation of Radiation*, F.G. Smith, ed. (SPIE Optical Engineering Press, Bellingham, Washington, 1993).

## 5.0 Imaging System Conceptual Design

### 5.1 Introduction

In this section of the report we consider the feasibility of four candidate imaging modalities for the LRLI sensor. These candidates are: conventional imaging, compensated imaging, scanner-based imaging and non-conventional (pupil-plane) imaging. Conceptual designs for these modalities along with discussions of their feasibility and performance are given in consecutive sections below. In section 4.6 a recommendation for the modalities that warrant further analysis is given.

### 5.2 Conventional Imaging

A simplified block diagram for a conventional LRLI sensor is shown in Fig. 5-1. This sensor consists of a laser transmitter, which as discussed in Section 3, should be a pulsed solid-state laser operating in the 1.5 - 2.1  $\mu\text{m}$  range with a pulse energy of 20 - 100 J. The transmit telescope

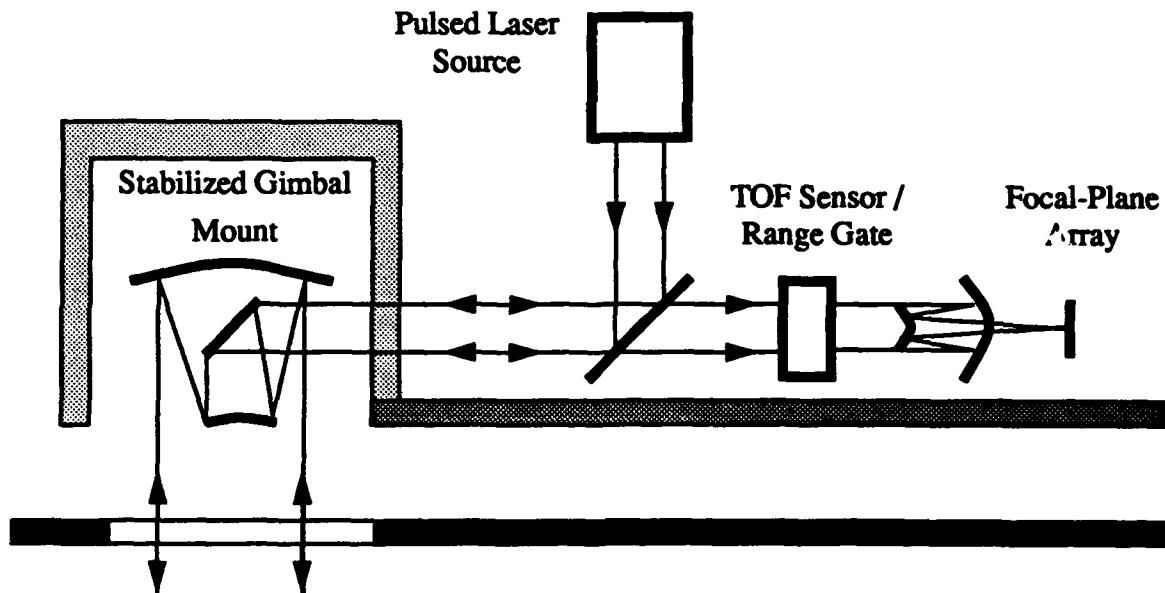


Figure 5-1. Block diagram of conventional LRLI sensor

is mounted on a stabilized Gimbal mount for pointing, tracking and stabilization. The return light is directed (this is typically done using polarization optics) to a TOF (Time-of-Flight) sensor and range gate. The TOF sensor determines when the light from the target returns and opens the range gate. The light then passes to an imaging telescope and on to a focal plane array. This array must be sensitive to the transmit wavelength. Candidate focal planes include InSb (Indium-Antimonide) and MCT (Mercury-Cadmium-Telluride).

Regarding feasibility, this sensor has the lowest risk of all being considered. Of its components, the most difficulty is associated with the range gate. This would be ideally accomplished with an electro-optic shutter. One other option would be to gate the focal plane electronically.

The performance of this sensor is also expected to be excellent. Adaptive optics are not used, but as shown in Section 4, they are not needed to obtain ground resolution of 1 meter. Also the optical system is relatively simple and thus transmission loss is minimized.

### 5.3 Compensated Imaging

A block diagram for a compensated LRLI sensor is shown in Fig. 5-2. This sensor is essentially the same as the conventional imaging sensor except that a wavefront sensor and

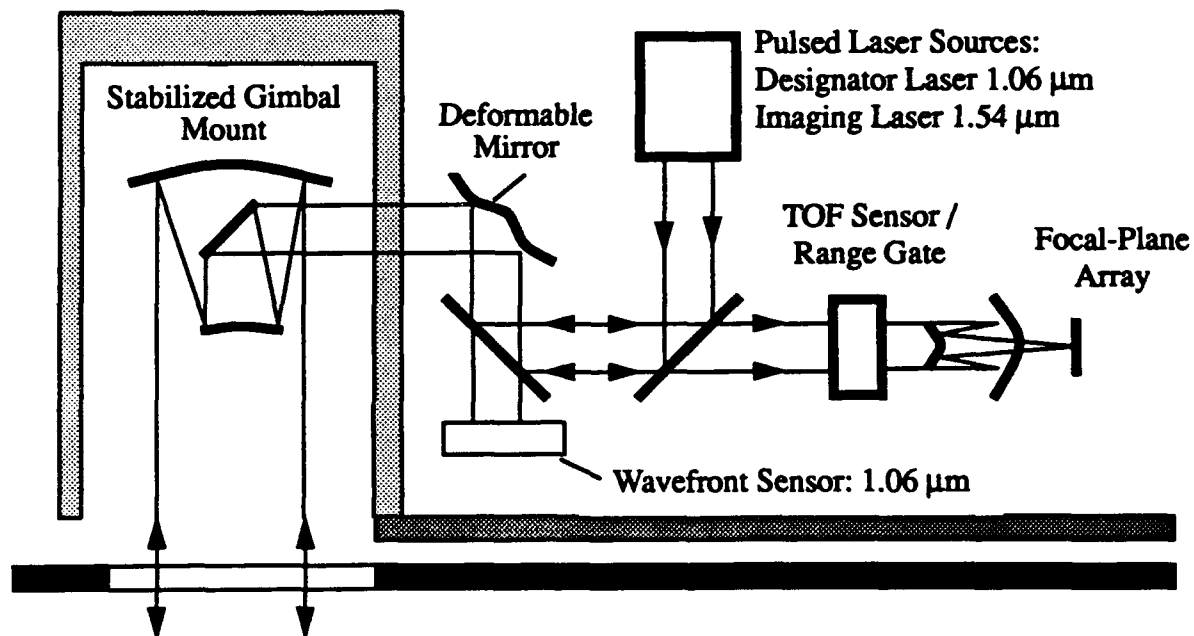


Figure 5-2. Block diagram of compensated LRLI sensor

deformable mirror are added. Conceptually this sensor has the feature that the designating laser beam can act as the "guide-star" for the wavefront sensor. Although this idea is conceptually appealing, in practice, the compensation capability is not required, and the sensor thus has unnecessary complexity.

Regarding this sensor's feasibility, the largest risk is associated with the compensated imaging. Particularly, the bandwidth of the system must be greater than the Greenwood frequency, which was calculated in Section 4 to be roughly 500 hz. Furthermore, anisoplanatism limits causes the correction to cover a very limited field-of-view, and thus a series of deformable mirrors is perhaps required.

As shown in Section 4, the imaging performance of this sensor is likely to be lower than that of a conventional imaging sensor because of the anisoplanatism. If the correction for one point on the ground is applied to the deformable mirror, it will add phase error to image points outside of the isoplanatic area. Furthermore the light efficiency of this system is lower than that of a conventional imaging system because of the increased number of optical components.

## 5.4 Scanner

Figure 5-3 contains a block diagram for a scanner embodiment of an LRLI sensor. This

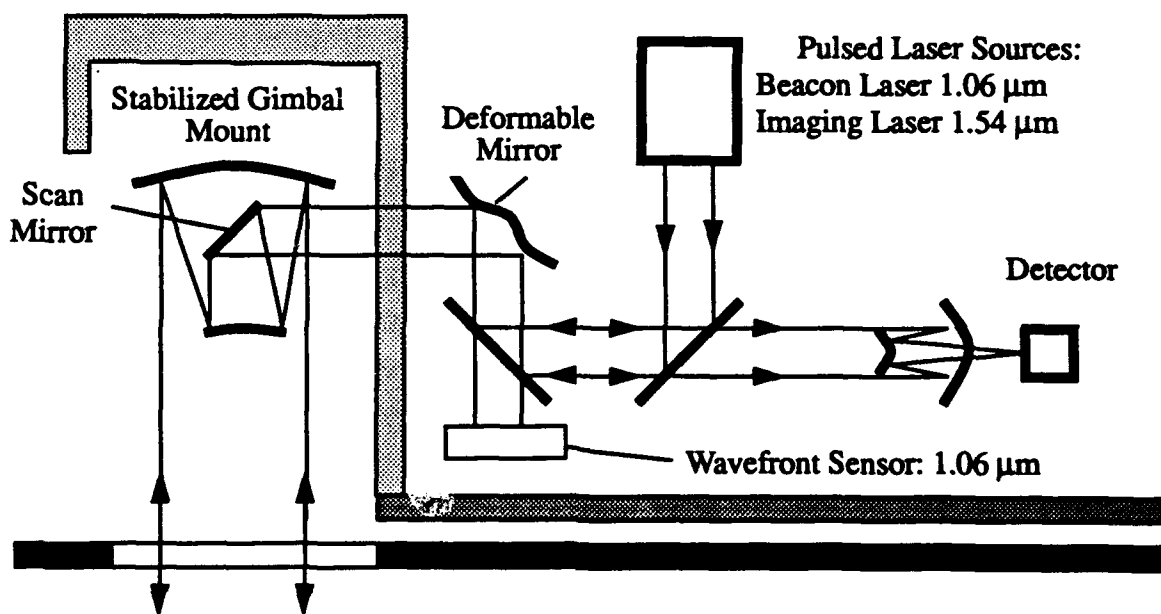


Figure 5-3. Block diagram of LRLI scanner.

sensor illuminates, and receives return, from one image point at-a-time. The 2-D image is synthesized with a 1-D scan mirror and 1-D platform motion, or 1-D gimbal motion.

As shown, this sensor has atmospheric compensation, however, as discussed above, it is likely to be unnecessary because of the relatively large  $r_0$  values encountered. Nonetheless, this sensor does offer a solution to the severe anisoplanatism by treating the image points serially. It is envisioned that the beacon laser will be sensed by the wavefront sensor, which will correct the beam for each image point. If compensated imaging is used, the pixel rate of this sensor is limited by the bandwidth of the compensated imaging system; for example if the bandwidth is 1000 hz, then the sensor could image 1000 points per second. It would thus take 10 sec to synthesize a 100 x 100 pixel image.

Perhaps the most important feature of this sensor is that it provide a convenient method for accomplishing range-gating. With a single detector, the return is sensed for an extended period and the peak return value, which corresponds to the ground return, is extracted. As stated in Section 5.2, range gating with an array can be challenging. One other feature of the scanner is that because the laser is fired once per pixel (instead of once per frame for a conventional imager) the laser power per pulse is lower, but the average power is maintained.

## 5.5 Pupil-Plane Imaging

With conventional imaging methods, an image is formed by using a lens to collect light and focus it onto a detector array located in the image plane. Performance of conventional imaging sensors is controlled by two key factors. First, resolution is limited by the size of the optical aperture, and, second, the ability to achieve diffraction-limited performance is dependant on the amount of atmospheric turbulence, particularly atmospheric turbulence in the pupil plane of the imaging system.

Researchers have developed methods for overcoming the performance limitations of conventional imaging methods. These methods include adaptive optical methods and pupil-plane methods. With adaptive optics, as discussed above, a wavefront sensor and deformable mirror are used to cancel the effects of atmospheric turbulence located in the pupil-plane of the imaging lens. Pupil-plane methods are used not-only to remove atmospheric turbulence, but also to synthesize larger optical apertures to get fine spatial resolution. In this report we are concerned with pupil-plane methods and not adaptive optical methods.

Pupil-plane imaging methods have received great attention for application to the problem of imaging satellites from the ground-based telescopes. Both the ability to synthesize large apertures, and the ability to overcome atmospheric turbulence are of importance for imaging of satellites. For the LRLI application, the ability to synthesize large apertures is not essential because real apertures can give sufficient resolution. For example, a 0.1 m aperture operating at a range of 100 km and wavelength  $1\mu\text{m}$ , would give spatial resolution of 1.0 m, which is sufficient for many applications. The remaining motivation to use pupil plane imaging is to negate atmospheric turbulence. This motivation, however, is weak, because the phase aberrations are not expected to be significant over the aperture. Nonetheless, we will continue with this discussion of pupil-plane imaging.

Before discussing the specific pupil-plane imaging methods, let us establish some geometrical parameters for the LRLI sensor which are shown in Fig. 5-4. The sensor platform flies at an expected altitude of 13 km. In Section 3.2, it was determined that a 20 J laser could image a scene area of roughly 100 m by 100 m measured perpendicular to the sensor line of sight. With the target range being typically 100 km, it follows that the depression angle of the scene is 7.4 degrees. As shown in the figure, the range extent of the scene (scene length along the sensor line-of-sight) is thus 769 m and the imaging area projected onto the ground is 775 m (cross-track) by 100 m (along track).

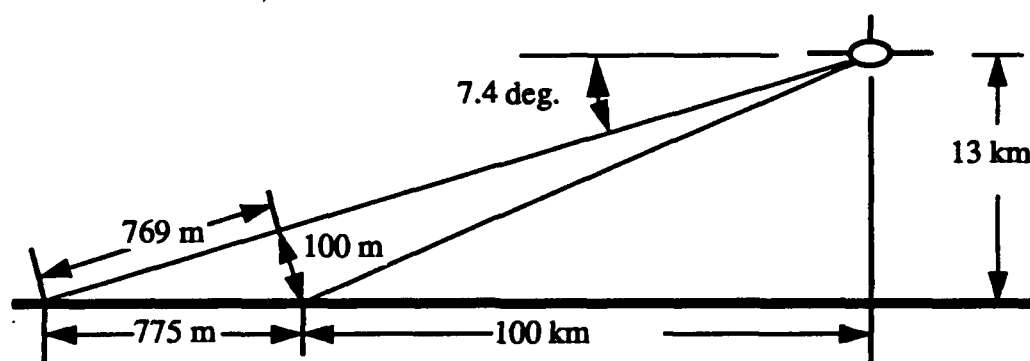


Figure 5-4. Sensor geometry.

Over the years, many pupil-plane imaging methods have been proposed. For this discussion, we will consider three methods. These are: imaging correlography, sheared beam, and laser

SAR. Descriptions of each of these methods and implications for the LRLI sensor are given below.

**Imaging Correlography** - For imaging correlography [5.1], the target scene is flood illuminated with light from a coherent laser source and a series of speckle intensity patterns are recorded over an area corresponding to the pupil plane of an imaging telescope. The method is insensitive to atmospheric turbulence because intensity detection in the pupil plane is used. The Fourier transform of an individual speckle pattern yields a speckled version of the autocorrelation of the object field. One can then average a series of these autocorrelations, from a series of laser pulses, to obtain a speckle-free version of the object autocorrelation. Phase-retrieval methods, with positivity and support (outline of illuminated region) constraints, can then be used to recover an image. Note that one can also apply phase-retrieval methods to recover a coherent image from a single speckle pattern, however, it is not as robust as imaging correlography partly because a positivity constraint cannot be invoked.

Some of the requirements for imaging correlography to work robustly are:

*Temporal Coherence* - The laser source must be temporally coherent over twice the range extent of the target. This corresponds to 1550 m for the example shown in Fig. 5-4.

*Integration Time* - The speckle pattern detected must be frozen spatially and not blurred by platform motion. Also, the detector integration time must correspond to an interval for which the entire target scene is illuminated with the laser pulse.

*Other* - It may be required that the support of the illuminated region have a shape that facilitates robust phase retrieval.

**Sheared-Beam** - The sheared-beam imaging method [5.2] allows image recovery from a single pupil-plane speckle pattern without the use of phase retrieval. The target is illuminated with two spatially separated beams of laser light that originate from the same laser. The pupil-plane intensity pattern (which is insensitive to atmospheric turbulence) is detected; this pattern corresponds to a sheared interferogram of the pupil-plane optical field. A phase-reconstruction algorithm can then be used to recover a coherent image.

Requirements for sheared-beam imaging are the same as for imaging correlography except that there are no restrictions on the object support.

**Laser SAR** - Laser imaging methods that are derived from conventional Synthetic Aperture Radar (SAR) imaging can also be employed [5.3]. For such a system the target is flood illuminated with an FM laser beam that is modulated with a chirp waveform. The return beam is then mixed with a local oscillator beam in the pupil-plane and the light is detected with a 1-D detector

array using heterodyne methods. A single point detector could also be used, however, because angular aperture synthesis is not required for this application a 1-D detector array is specified because it would be more robust. The 1-D detector array provides pupil-plane Fourier fill in the angle dimension, and the chirped waveform provides Fourier fill in the range dimension. Fourier transformation of this data yields a range-angle image of the illuminated scene. The resulting image is analogous to a SAR image.

Requirements for laser SAR are more stringent than for the other two imaging modalities discussed above. The requirements include the following:

*Temporal Coherence* - The illumination must be spatially coherent over the extent of the scene. In addition the temporal coherence length of the laser must ideally encompass the round-trip propagation path of the light (200 km), however, this requirement might be relaxed by advanced processing methods.

*Temporal Integration* - The speckle pattern must ideally be frozen over the entire chirped waveform, however, this requirement may be relaxed by formatting the data in a parallelogram shape. The detector integration time must correspond to a time interval over which the entire scene is illuminated with an individual laser frequency.

*Other* - This sensor is sensitive to phase aberration imparted by the atmosphere. Advanced processing algorithms can be used to remove atmospheric phase aberration. Because heterodyne detection is used, extreme optical and mechanical precision must be incorporated into the sensor design.

Let us now consider the ability of the LRLI sensor to meet the requirements for the various pupil-plane imaging modalities. One key area for consideration is the laser illuminator. Pupil-plane imaging methods require temporal coherence lengths of 1550 m for the sensor geometry shown in Fig. 5-4. This is significantly longer than the available values. Note that laser SAR methods may require even longer source coherence lengths, roughly 200 km, which are even less feasible.

For temporal integration time, the most basic requirement is that the speckle pattern be frozen over the detector integration time, and that the entire scene be illuminated during this interval. As the aircraft flies along, it follows that the speckle pattern changes in time. If we adopt the simplifying assumption that the scene is perpendicular to the line of sight, the speckle pattern

translates bodily at twice the platform velocity and in the opposite direction relative to platform coordinates [5.5]. It follows that the speckle rate is given by

$$\text{Speckle Rate} = \frac{\text{Speckle Velocity}}{\text{Speckle Size}}$$

With the speckle size given by  $\lambda R/D$ , where  $\lambda$  is the source wavelength,  $R$  is the target range and  $D$  is the diameter of the illuminated region, the speckle rate is given by

$$\text{Speckle Rate} = \frac{2VD}{\lambda R}$$

With  $V = 231.5$  m/sec (from above),  $D = 100$ m,  $\lambda = 1\mu\text{m}$  and  $R = 100$  km, the speckle rate is  $0.463 \times 10^6$  speckles/sec. If we assume that the detector can integrate for one fourth of the speckle lifetime, the maximum detector integration time is  $0.54 \mu\text{sec}$ .

One other aspect of the detector integration time is that the entire scene must be illuminated while the detector integrates. To satisfy this requirement, the scene must be illuminated for a duration of  $5.17 \mu\text{sec}$  (time for light to travel  $1520$  m) before the detector can begin to integrate. Once the  $5.17 \mu\text{sec}$  has passed, the sensor can integrate for a maximum of  $0.54 \mu\text{sec}$ , as dictated by the speckle dynamics. Timing for the pulse is illustrated in Fig. 5-5 below. The scene is illumi-

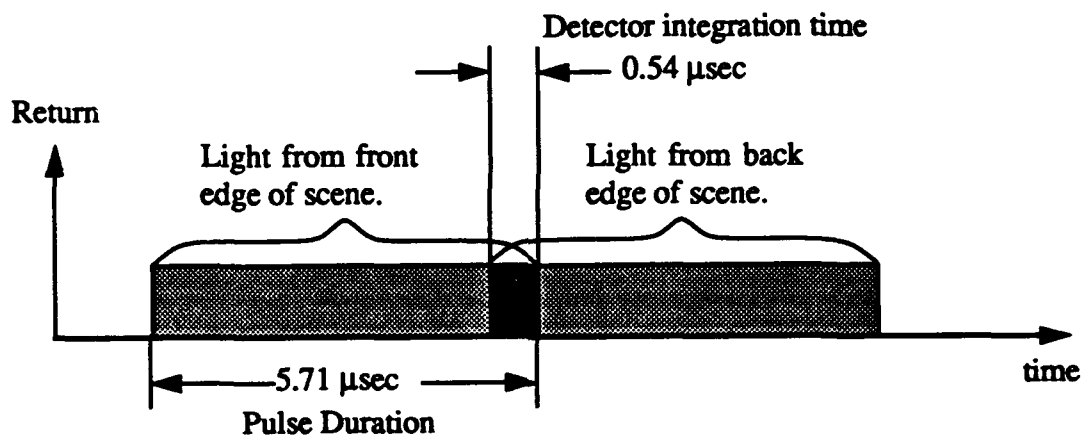


Figure 5-5. Illumination pulse timing.

nated with a temporally coherent pulse of duration  $5.71 \mu\text{sec}$ . With light from the leading and trailing edges of the scene present, the detector then integrates for  $0.54 \mu\text{sec}$ . Note that these timing issues result in only 10 percent of the light being useful. This is an important limitation of these pupil-plane imaging methods. Note that for the calculations of signal level given in Section

3.2, this factor of 10 percent was not included; with this factor, a 200 J laser would be required to image an area with 100 m along track size.

In summary, it has been shown that for the LRLI sensor geometry, pupil-plane imaging methods require very long laser coherence lengths ( $> 1$  km) which is beyond the current capability for high-power illuminators. Also, there is a significant energy loss factor caused by the requirement that the entire scene be illuminated simultaneously with the sensor integration time being a fraction of the speckle lifetime. These factors result in the determination that the considered pupil-plane imaging methods are not applicable for the LRLI sensor. Instead, other non-conventional imaging methods, such as adaptive optics should be considered.

## 5.6 Recommendation

The two sensor types that warrant further investigation are 1) a conventional imaging system with pulsed illumination and range-gated detection and 2) a scanner system that does not include atmospheric compensation. The scanner is attractive because range gating is readily accomplished with the single detector. This recommendation is influenced heavily by the large anticipated values of  $r_0$  and the small isoplanatic angle.

## 5.7 References

- [5.1] P. S. Idell, J. R. Fienup and R. S. Goodman, "Image synthesis from non-imaged laser speckle patterns," *Opt. Lett.* **12**, 858-860 (1987).
- [5.2] Briefing materials from - Active Imaging Testbed Pre-Solicitation Conference, Jan. 15, 1993, Phillips Laboratory, Kirtland AFB, N.M.
- [5.3] C. C. Aleksoff, J. S. Accetta, L. M. Peterson, A. M. Tai, A. Klooster, K. S. Schroeder, R. M. Majewski, J. O. Abshier, and M. E. Fee. "Synthetic aperture imaging with a pulsed CO<sub>2</sub> TEA laser," in *Laser Radar II*, R.J. Bercherer and R.C. Harney, eds., *Proc. SPIE* **783**, 29-41 (1987).
- [5.4] J. C. Marron and K.S. Schroeder, "Speckle from rough, rotating objects," *Appl. Opt.* **27**, 4279-4287 (1988).

## 6.0 Long-Range Designator Performance

### 6.1 Introduction

In this section of the report we evaluate the performance of a long-range laser designator. This analysis includes calculations of the SNR for a laser designator as a function of range. Key technical issues are also discussed.

### 6.2 Performance Prediction

An illustration of the scenario for long-range laser designation is shown in Fig. 6-1. This illustration shows the LRLI platform, which is a high-flying platform that contains the designating laser. The designating laser illuminates a target and the beam reflects from the target. A portion of the reflected light is received by a low-altitude platform that has a laser-guided weapon.

It is envisioned that the LRLI platform would be flying at a safe distance from enemy threats and would have time to interrogate a target region to locate a specific target. Once a specific target is located, a fighter aircraft with a laser-guided bomb is sent into the area. At this time the target is designated with a small diameter laser beam from the long-range platform. Once the fighter platform determines that the weapon is locked onto the designating beam, the weapon is

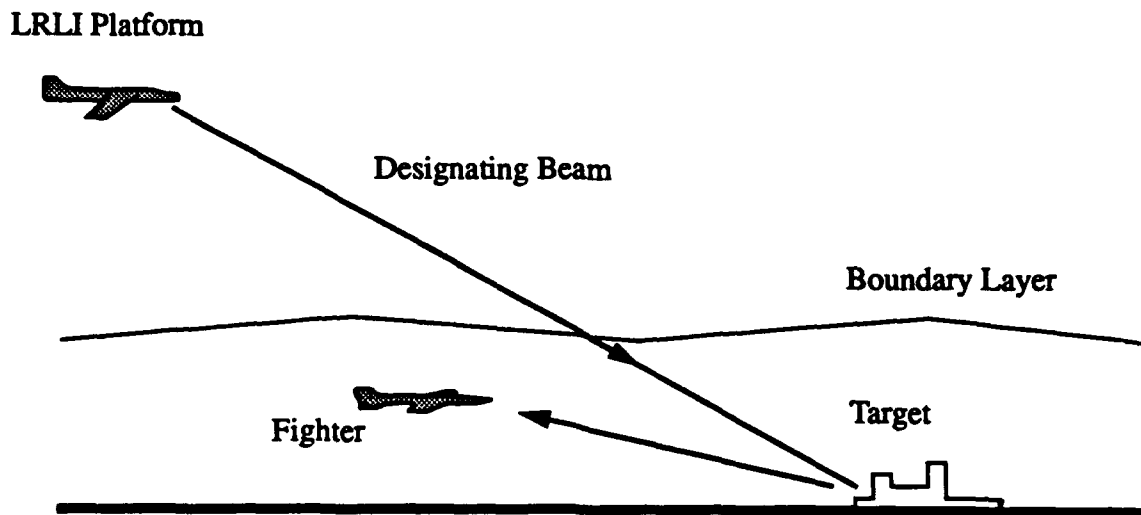


Figure 6-1. Illustration of Scenario for Long-Range Imaging.

released. The fighter then leaves the area and Bomb-Damage-Assessment (BDA) is performed by the long-range platform.

This long-range designation has several advantages over conventional designation, for which designation and weapon delivery are conducted by the same close-range, fighter aircraft. These advantages include the increased time interval available for the long-range platform to perform interrogation, targeting and BDA. Also the fighter aircraft is exposed to enemy fire for a shorter time interval, thus increasing aircraft and crew survivability. These factors are also discussed in Section 2.0 above.

In order to perform robustly, the laser-guided weapon must receive a strong and consistent return from the designated target. Signal strength is driven by the laser power and other factors such as atmospheric transmittance and beam divergence. Consistency of the return is affected by factors such as jitter and motion of the designator spot.

For the long range scenario, the absorption of light occurs mainly in the boundary layer of the atmosphere (lowest 2 km) as discussed in Section 3. For this analysis we will treat the atmospheric absorption of the paths to and from the target separately. Because the path to the target occurs mainly above the boundary layer, we treat it as a constant that is independent of the distance from the designator platform to the target. The path from the target to the weapon occurs mainly within the boundary layer, and thus we will use a Beer's law treatment. As a result, the SNR for a laser designator is given by [6.1]

$$SNR = \frac{E_L \eta_B \rho \tau_{LR} e^{-(\kappa R)}}{NEI t \pi R^2}$$

where  $E_L$  is the laser energy per pulse,  $\eta_B$  ( $= 0.8$ ) is the fraction of the designator beam that is within the weapon's FOV,  $\rho$  ( $= 0.1$ ) is the target reflectance,  $\tau_{LR}$  ( $= 0.1$ ) is the transmittance of the atmosphere from the designating platform to the target,  $\kappa$  is the absorption coefficient for the path from the target to the weapon,  $R$  is the distance from the target to the weapon.  $NEI$  is the noise-equivalent irradiance of the weapon's receiver, and  $t$  is the laser pulse duration.

Consider a designator that operates at  $1.54 \mu\text{m}$  with a pulse energy of 15 mJ and 10 nsec pulses. Note that the pulse energy is very modest compared to the energy required for long-range imaging. From Ref. [6.1], the NEI for this class of sensor is  $1.43 \times 10^{-6} \text{ W/m}^2$ . As discussed in Section 3 we will take the absorption coefficient for the atmosphere to be  $\kappa = 0.0438 \text{ km}^{-1}$  for a clear atmosphere and  $\kappa = 2.937 \text{ km}^{-1}$  for thin fog [6.1]. Plots of SNR versus weapon range are given in Fig. 6-2. Notice that the SNR value is less than 10 at a weapon range of 15 km for a clear atmosphere. Also note that these results are affected drastically by the presence of fog.

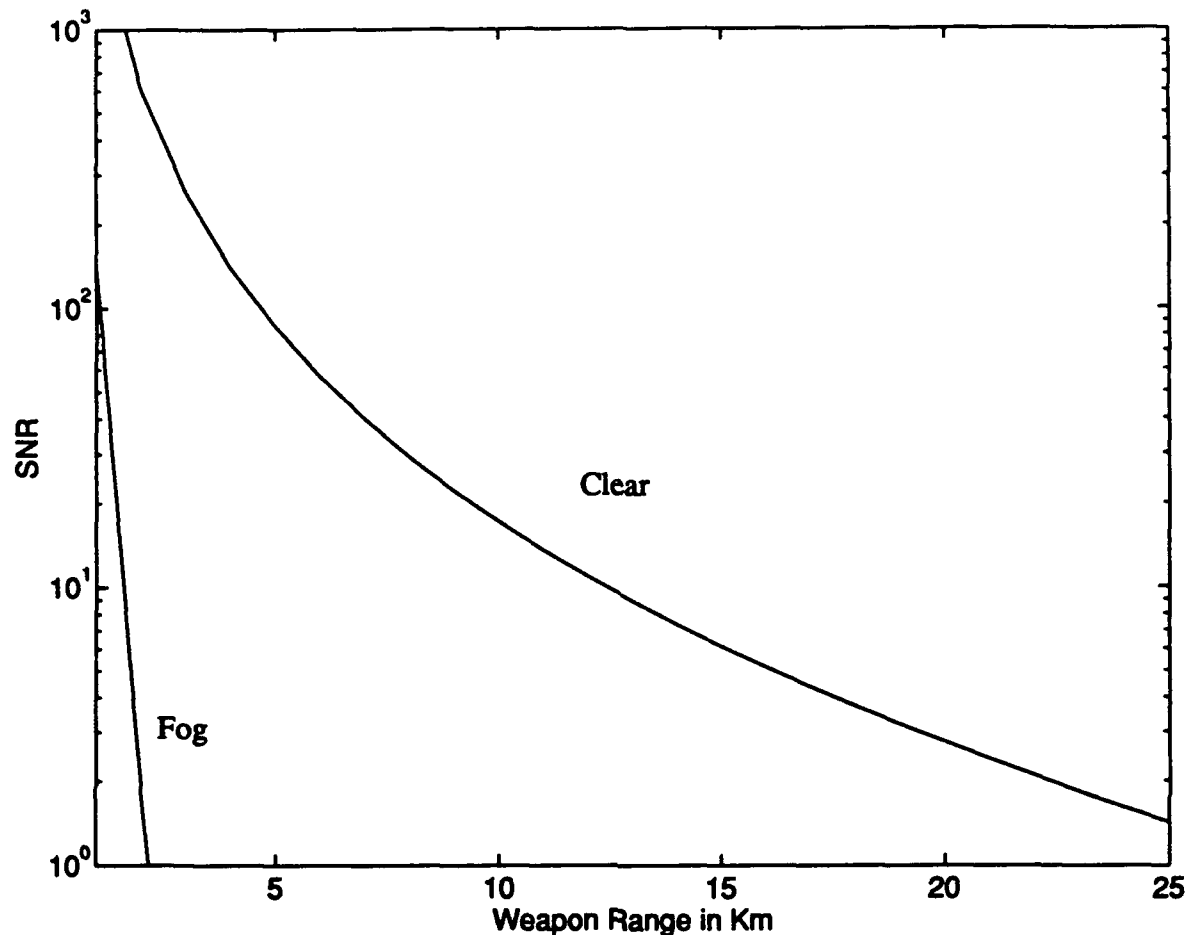


Figure 6-2. SNR for Laser Designator Versus Range in km.

It is important to note that the results shown in Figure 6-2 apply to the scenario shown in Fig. 6-1. In certain circumstances one may be interested in the monitoring the location of the designating spot from the designating platform. In this case the analysis given in Section 3.2.5 should be applied; the signal level is dominated by the  $1/R^2$  dependence of the return level.

### 6.3 Reference

- [6.1] R. W. Byren, "Laser Rangefinders," in *The Infrared & Electro-Optical Systems Handbook, Volume 6: Active Electro-Optical Systems*, C. S. Fox, ed. (SPIE Optical Engineering Press, Bellingham, Washington, 1993).

## 7.0 Recommendation for Experiments

### 7.1 Introduction

In the previous sections of this report, we have shown that the LRLI sensor concept is feasible. Here we discuss possibilities for proof-of-concept experiments. The most favorable embodiment for the sensor is conventional imaging (no adaptive optics) with pulsed-illumination and range-gating as shown in Fig. 7-1. The laser would ideally be a pulsed laser that operates near 2  $\mu\text{m}$ . Operation at this wavelength minimizes loss due to scatter and is eyesafe. This pulsed laser would flood illuminate a target region and a portion of the reflected light would be intercepted by the receiver aperture. The focal-plane-array would be range-gated so that it collects reflected light from the target, and the contribution of background is minimized. While there are several approaches for range-gating, it appears that the best approach for the proposed experiments is electronic range gating. In this manner, the sensor integrates only for a short time interval over which laser light returns from the target. Typical values for the minimum integration interval are in the 1 - 10  $\mu\text{sec}$  range.

There are several candidate locations for performing the experiments. These are discussed in the following section.

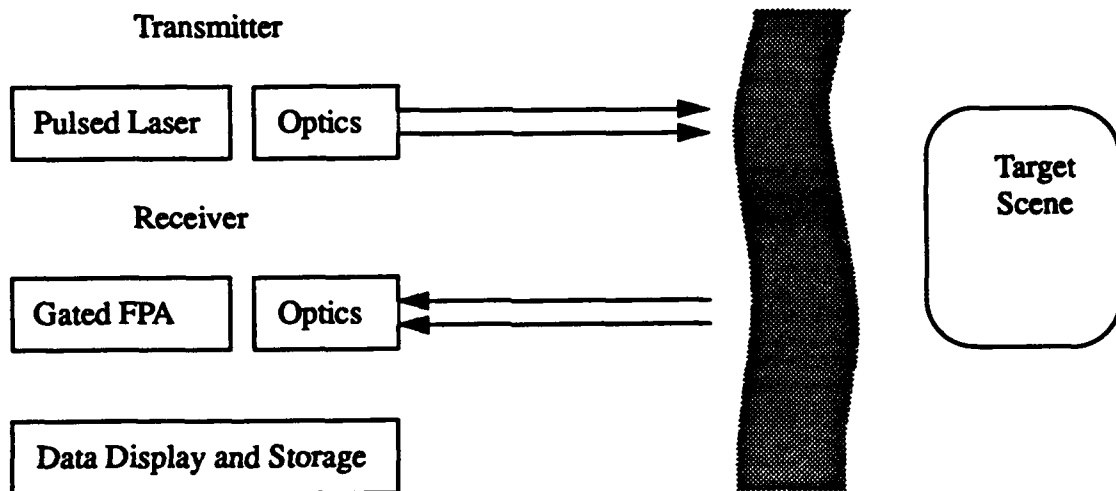


Figure 7-1. Block Diagram for Proof-of-Concept Experiments.

## 7.2 Proof-of-Concept Experiment Locations

The favored location for conducting the experiments is from a mountain top looking down. Such a site provides for essentially unlimited sensor size weight and power and avoids the expense associated with flying a sensor in an airplane. The leading candidate of mountain top locations is Mt. Heliacal which is on the island of Maul, Hawaii. At this location there are several possible ranges to target scenes as shown in Fig. 7-2. One minor concern about this location is that the sensor altitude (3 km) is not much higher than the boundary layer (2 km). This site will thus exhibit different atmospheric absorption and turbulence properties than the long slant-range path from a high altitude aircraft. For example, absorption for the 15 km path shown may be as severe as the entire 100 km path for a high-altitude sensor. An important aspect of the experimental design is that the geometry chosen must give atmospheric conditions that are scientifically scalable to the high-altitude case.

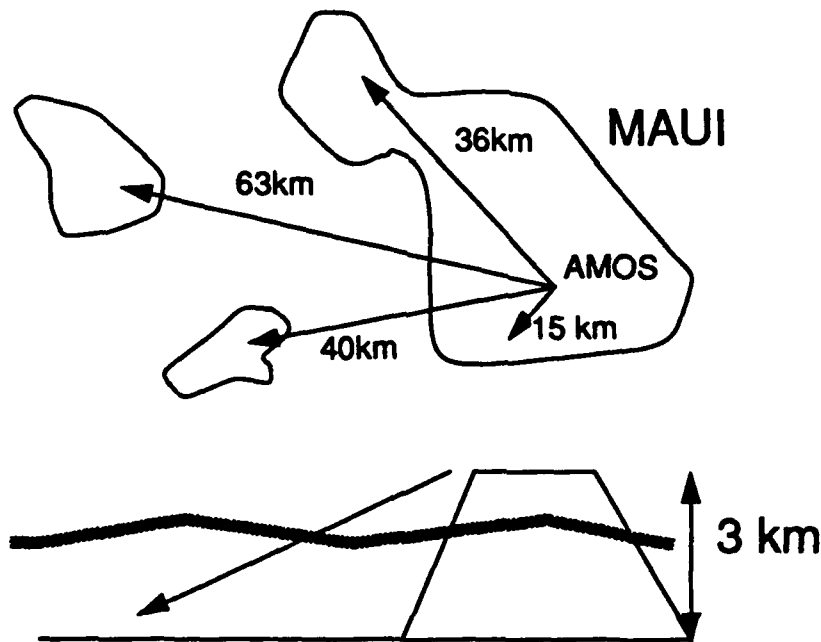


Figure 7-2. Illustration of Possible Imaging Locations from Mt. Haleakala.

One other candidate sensor location is to fly the sensor on a hot-air balloon [7.1]. One current balloon in the Air Force inventory is illustrated in Fig. 7-3. This balloon is capable of flying to an altitude of 24 Kft and has a tethered generator with 2.2 Kwatt capacity. A variety of optical

and infrared sensors have been flown on this platform. In order to fly an LRLI sensor in the balloon, the sensor would have to satisfy demanding size, weight and power constraints. These constraints would be expensive to conform to, while retaining sensor performance. At this point in the LRLI sensor's development, the mountain-top approach is preferred.

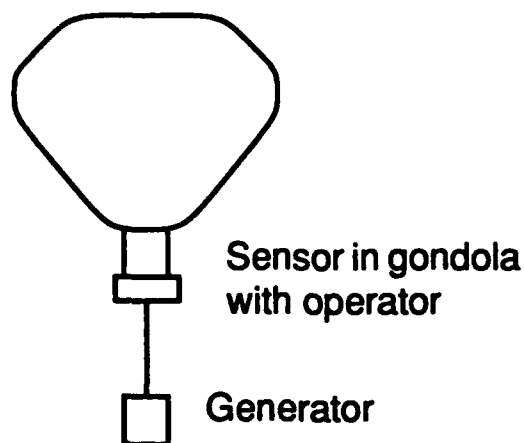


Figure 7-3. Illustration of Hot-Air Balloon Approach for LRLI Sensor Development.

The final candidate location for LRLI sensor demonstration is on board an aircraft. The cost associated with this aircraft demonstration, however, is prohibitive at this point. Such airplane demonstration will be required as a later stage in the development of the LRLI sensor.

### 7.3 Reference

7.1 Private communication with Lt. Col. Steve Watson, Hill AFB, Utah (801)777-2016.